Monthly Notices
of the
ROYAL ASTRONOMICAL SOCIETY

MNRAS **541,** 3280–3306 (2025)
Advance Access publication 2025 July 12

https://doi.org/10.1093/mnras/staf1145

Investigating field burial by magnetically confined accretion mounds on neutron stars

Saurabh Yeole ,[1★] Dipanjan Mukherjee [1★] and Ankush Mandal [1,2]
[1] *Inter-University Centre for Astronomy & Astrophysics, Post Bag 4, Ganeshkhind, Pune 411007, India*
[2] *Leibniz-Institut für Astrophysik Potsdam (AIP), An der Sternwarte 16, D-14482 Potsdam, Germany*

Accepted 2025 July 10. Received 2025 July 10; in original form 2025 April 3

ABSTRACT

We explore the problem of magnetic confinement of accreted matter forming an accretion mound near the magnetic poles of a neutron star. We calculate the magnetic field geometry of the accreted mound by solving the magnetostatic Grad Shafranov (GS) equation in radially stretched spherical coordinates with high resolution and an extended domain. In this work, we propose a new physically motivated multipolar current free boundary condition at the outer radial boundary. We have evaluated a large suite of GS solutions for different neutron star magnetic fields and mound configurations. We find that with sufficient resolution, the ring-shaped mound profiles spread latitudinally on the neutron star surface, towards the equator, with a potential decline in dipole moment at outer radii, demonstrating the onset of field burial. A higher latitudinal spread towards the equator leads to more effective magnetic field burial. Along with the ring-shaped mound profile on a hard crust majorly used in this work, we also model mounds formed on a pre-existing ocean, which is more physically motivated. Additionally, we explore different GS solutions for a quadrudipolar surface magnetic field. We find that such configurations lead to asymmetric polar mounds. We discuss the validity of such solutions for different relative strengths of the quadrupole and dipolar components.

Key words: stars: neutron – magnetic fields – accretion – methods: numerical.

1 INTRODUCTION

Neutron stars are known to have two distinct populations in terms of their surface magnetic fields, viz. low magnetic fields of $\sim 10^8$–10^{10} G such as in millisecond pulsars, and those with higher magnetic fields ($\gtrsim 10^{12}$ G), comprising of the bulk of known neutron star population (see Konar 2017, and references therein). An accretion induced reprocessing scenario is often invoked to explain both the higher spin frequencies and lower magnetic field in millisecond pulsars. Although long-term accretion-driven spin-up has now been generally accepted as the cause of origin of such sources (Smarr & Blandford 1976; Alpar et al. 1982; Radhakrishnan & Srinivasan 1984), the reason for low magnetic fields in such systems has not been understood yet. Several mechanisms have been proposed for this, such as surface magnetic field burial in the crust due to the accreted matter (Romani 1990; Cumming, Zweibel & Bildsten 2001; Melatos & Phinney 2001; Choudhuri & Konar 2002; Konar & Choudhuri 2004; Payne & Melatos 2004, 2007), high crust resistivity due to accretion induced heating (Urpin & Geppert 1995; Konar & Bhattacharya 1997; Urpin & Konenkov 1997; Konar & Bhattacharya 1999a), fluxoid-vortex migration to the crust (Muslimov & Tsygan 1985; Srinivasan et al. 1990; Jahan Miri & Bhattacharya 1994; Konar & Bhattacharya 1999b), crustal magnetothermal evolution (Blondin & Freese 1986), crustal tectonic motions (Ruderman 1991a, b), vortex destruction due to accretion induced currents (Istomin & Semerikov 2016), and screening of core magnetic field generating currents by accretion induced currents (Arons & Lea 1980). Magnetic field burial due to accreted matter has been one of the widely studied problems explored previously by various authors without a resolution to the issue.

Matter accreted on the neutron star could also contribute to the emission of continuous gravitational waves (CGW; Melatos & Payne 2005; Singh et al. 2020; Sur & Haskell 2021b; Rossetto, Frauendiener & Melatos 2025), which has served as another strong motivation for studying the feasibility of forming magnetically confined mounds,[1] on neutron stars. Neutron star deformation due to magnetic stresses can also lead to the emission of CGW (Bonazzola & Gourgoulhon 1996; Mastrano, Suvorov & Melatos 2015; Chatterjee, Novak & Oertel 2021; Sur & Haskell 2021a). The various other sources of CGW from isolated neutron stars could be from quakes due to cooling and cracking of the crust (Pandharipande, Pines & Smith 1976; Kerin & Melatos 2022), changing centrifugal stress induced by stellar spindown (Baym et al. 1969; Ruderman 1969; Fattoyev, Horowitz & Lu 2018; Giliberti & Cambiotti 2022), non-axisymmetric distribution of magnetic energy trapped beneath the crust (Zimmermann 1978; Cutler 2002), pinned neutron superfluid

---

★ E-mail: saurabh.yeole@iucaa.in (SY); dipanjan@iucaa.in (DM)

[1] Instead of 'mounds', the term 'mountains' have also been used in literature to describe the magnetically confined accreted matter on neutron stars.

component in the star's interior (Jones 2010; Melatos, Douglass & Simula 2015; Haskell, Antonelli & Pizzochero 2022), r modes (Owen 2010; Alford & Schwenzer 2014; Mytidis, Coughlin & Whiting 2015), high-frequency f modes (Chandrasekhar 1970; Friedman & Schutz 1978; Lindblom & Mendell 1995), or excitation of r modes due to accretion (Bildsten 1998). See Riles (2023) for a recent review on efforts to detect CGW from rotating neutron stars.

Bisnovatyi-Kogan & Komberg (1974), Blandford, Decampli & Konigl (1979), and Taam & van den Heuvel (1986) were some of the first few proponents of the idea of diamagnetic screening due to accreting matter. Later, brief semi-analytical calculations were presented by Hameury et al. (1983), Brown & Bildsten (1998), Melatos & Phinney (2001), and Choudhuri & Konar (2002). One of the first detailed self-consistent solutions to demonstrate field reduction due to magnetic confinement of accreted matter was by Payne & Melatos (2004). The authors developed a numerical method to solve a dimensionless Grad Shafranov (GS) equation for solutions of the hydromagnetic equilibria of accreted matter on the neutron star. Using an isothermal equation of state (EOS[2]) for the accreted plasma, the authors obtained masses as large as 10^{-4} $M_{\odot}$. These solutions were improved by Priymak, Melatos & Payne (2011) and Priymak, Melatos & Lasky (2014), who tested the mounds for an adiabatic EOS and $B = 10^{12.5}$ G. Similar to earlier results, they showed that the characteristic mass at which the outer radius dipole moment reaches 50 per cent of the surface dipole moment is 5×10^{-4} $M_{\odot}$ for isothermal EOS. However, solutions with a more physically motivated Fermi gas EOS yielded much lower limits such as 10^{-7} $M_{\odot}$ for relativistic degenerate electron EOS and 3×10^{-8} $M_{\odot}$ for non-relativistic degenerate electron EOS. A limitation of these works is that the assumed mound profile loads matter on to the magnetic field lines from the pole to the equator. In a realistic system, the accreted matter should only be loaded near the magnetic pole up to the magnetic field line attached to the inner cut-off radius of the accretion disc.

GS solutions with mounds restricted to a polar cap radius defined by Alfvén radius were performed by Mukherjee & Bhattacharya (2012), Mukherjee, Bhattacharya & Mignone (2013a), and Mukherjee (2017). These solutions demonstrated much lower confined masses ($\lesssim 10^{-12}$ $M_{\odot}$) beyond which viable converged solutions were not obtained due to the appearance of closed field loops in the compute domain (also reported in Hameury et al. 1983; Payne & Melatos 2004). Mukherjee (2017) provided a brief review of the work on field burial till 2017.

All of these works above have certain limitations (refer to the limitations in Mukherjee 2017). One of the deficiencies was the boundary condition at the outer radius of the simulation domain. Previous works have considered either a free boundary condition (Payne & Melatos 2004; Wette, Vigelius & Melatos 2010; Priymak et al. 2011; Suvorov & Melatos 2020), a fixed boundary condition (Mukherjee & Bhattacharya 2012; Mukherjee 2017) or a reduced dipole boundary condition (Rossetto et al. 2023) at the outer radial boundary. However, a boundary fixed to the dipolar value as used in Mukherjee & Bhattacharya (2012) is very restrictive and is not able to probe diamagnetic screening by design. On the other hand, a free boundary as in Payne & Melatos (2004, and later) leads to radial magnetic fields that may not be physical. The reduced dipolar boundary in Rossetto et al. (2023) addresses these issues to some extent, but still is limiting in nature, as it suppresses other multipoles from freely evolving.

Another limitation of the previous papers is that all the works discussed above had calculated solutions for high magnetic field pulsars. Recently, Fujisawa, Kisaka & Kojima (2022) solved the GS equilibria in spherical coordinates (similar to Payne & Melatos 2004) that included the effect of an axisymmetric toroidal field, with an arbitrary smooth source function profile. The authors numerically solved the integral form of the GS equation (accounting for the force-free nature of the magnetic field at the outer boundary) for a range of neutron star magnetic fields, and presented changes in mass-ellipticity and multipole moments of the magnetostatic mounds. However, a self-consistent evolution of the profile function duly accounting for the change in Alfvén radius due to varying magnetic fields was not considered.

Analysis of recent NICER observations suggests that pulsars have a complex non-dipolar magnetic field profile (Bilous et al. 2019; Chen, Yuan & Vasilopoulos 2020; Kalapotharakos et al. 2021; Riley et al. 2021). Fujisawa et al. (2022) calculated solutions for an initial dipolar field, an initial dipolar + quadrupolar field and an initial dipolar + octupolar field. Similar to the inferences of Suvorov & Melatos (2020), Fujisawa et al. (2022) found that for an initial dipolar field, the solutions show a buried dipole field and an increase in multipolar components. Fujisawa et al. (2022) also found that for an initial dipolar and strong multipole fields (10 times the dipolar field at the surface), the multipolar fields are buried and transformed into negative dipolar components. However, the authors considered only a single value for surface quadrupole to dipole fraction. Additionally, the authors did not account for a change in the Alfvén radius due to the new quadrudipolar magnetic field.

In this work, we address some of the limitations described above. We propose a new current free boundary (CFB) condition for the outer radial boundary and compare the results with other traditional boundary conditions. The solutions here have been carried out with improved EOS (Paczynski 1983; Mukherjee 2017) that better describes the pressure over a broader range of densities than a polytropic EOS used in previous works (e.g. Priymak et al. 2011; Mukherjee & Bhattacharya 2012) for the degenerate plasma. Using the above, we have computed a suite of GS solutions for different mound properties and neutron star conditions. The section-wise break-up is as follows. Section 2 describes the GS equation form solved here, the numerical method used to solve it, the EOS used, and the boundary conditions for the simulation domain and the parameter space explored here. Section 3 describes the form of the solutions for the ring-shaped mound profile and the effect of the boundary condition at the outer radius on the solution. We have calculated the ellipticity and dipole moments of the mounds for a range of magnetic fields (low field 10^9 G to high field 10^{12} G pulsars) with a mound profile duly accounting for the change in the Alfvén radius. We have also calculated the same for $B_d = 10^{12}$ G and an arbitrary truncation angle 50^0. Section 4 presents solutions and an analysis of the results for three different profile functions. Section 5 describes the form of the solutions for the ring-shaped mound profile for a quadrudipolar inner boundary. The final section summarizes all the results of the paper and discusses their implications. Thus, we present high-resolution simulations of accretion mounds with a larger domain, an improved multipolar CFB condition, new profiles and solutions for an initial quadrudipolar field.

---

[2] In this work, the term equation of state or EOS will be used to refer to the thermodynamic description of the accreted matter, and not the compositional description of matter interior to the neutron star crust used to solve for neutron star structures (Lattimer & Prakash 2004; Haensel, Potekhin & Yakovlev 2007).

2 ACCRETION MOUNDS

2.1 Grad Shafranov equation

Let the magnetic field vector, plasma pressure, plasma density, and gravitational potential be denoted by $\boldsymbol{B}$, p, ρ, and ϕ_g, respectively. From force balance in a neutron star plasma, we have

$$\frac{(\nabla\times\boldsymbol{B})\times\boldsymbol{B}}{4\pi}=\nabla p+\rho\nabla\phi_g. \tag{1}$$

Assuming axisymmetry and a zero toroidal magnetic field, we have

$$\boldsymbol{B}=\frac{\nabla\psi(r,\theta)\times\hat{\phi}}{r\sin\theta}, \tag{2}$$

where $\psi=r\sin\theta A_\phi$. Here (r,θ,ϕ) are spherical coordinates, ψ is the magnetic poloidal flux function and A_ϕ is the toroidal component of the magnetic vector potential. We assume the gravitational potential to be $\phi_g=gr$, where $g=GM_*/R_*^2$ is the constant gravitational acceleration due to the neutron star (G is the gravitational constant, M_* and R_* are the mass and radius of the neutron star respectively). Using the EOS, we can write $\nabla p=\rho\nabla G(\rho)$. Using equation (2), equation (1) can be rewritten as

$$-\frac{\Delta^2\psi}{4\pi r^2\sin^2\theta}\nabla\psi=\rho\nabla(G(\rho)+\phi_g) \tag{3}$$

where

$$\Delta^2=\frac{\partial^2}{\partial r^2}+\frac{\sin\theta}{r^2}\frac{\partial}{\partial\theta}\left(\frac{1}{\sin\theta}\frac{\partial}{\partial\theta}\right). \tag{4}$$

Defining r_0 as a function of ψ such that

$$\rho g\nabla r_0(\psi)=\rho\nabla(G(\rho)+\phi_g). \tag{5}$$

Rearranging, we get

$$\rho g\nabla(r_0(\psi)-r)=\rho\nabla G(\rho).$$

Integrating the above equation, we find

$$g(r_0(\psi)-r)=G(\rho)+C. \tag{6}$$

We assume $\rho=0$ at $r=r_0(\psi)$ and calculate C accordingly. $r_0(\psi)$ is analytically assigned to be a function of ψ such that it represents the radial extent of the mound for each flux surface. ρ is calculated by inverting equation (6). Substituting equation (5) in equation (3), we get

$$-\frac{\Delta^2\psi}{4\pi r^2\sin^2\theta}\nabla\psi=\rho g\nabla r_0(\psi)=\rho g\frac{dr_0}{d\psi}\nabla\psi. \tag{7}$$

The GS equation for zero toroidal field in spherical coordinates (r,θ) is (Payne & Melatos 2004; Mukherjee 2017)

$$\Delta^2\psi=K(\psi,r,\theta), \tag{8}$$

where

$$K(\psi,r,\theta)=-4\pi r^2\sin^2\theta\rho g\frac{\mathrm{d}r_0(\psi)}{\mathrm{d}\psi}, \tag{9}$$

$r_0(\psi)$ is a profile function which defines the shape of flux surfaces and Δ^2 is given by equation (4). To better resolve the strong gradients at the base of the mound and in the latitudinal direction, it is convenient to recast the GS equation in terms of new variables:

$$(r,\theta)\rightarrow\left(y=\log\left(\frac{r-aR_*}{R_*(1-a)}\right),\mu=\cos\theta\right). \tag{10}$$

The resulting GS equation is

$$\frac{\partial^2\psi}{\partial y^2}-\frac{\partial\psi}{\partial y}+\frac{(1-\mu^2)}{\left(1+\frac{a}{e^y(1-a)}\right)^2}\frac{\partial^2\psi}{\partial\mu^2}$$
$$=R_*^2(1-a)^2e^{2y}K(\psi,y,\mu). \tag{11}$$

Here, R_* is the radius of the neutron star in km and a is a parameter that defines the stretching of the grid. We use a= 0.999 for all simulations in this work (Appendix A).

2.2 Numerical method

We solve the GS equation through an iterative scheme using the successive overrelaxation (SOR) method. The solver has been updated to be compatible with Message Passing Interface (MPI), using a red-black parallelization scheme (Press et al. 1992). The details of the numerical scheme and the comparison with the previous results of Mukherjee (2017) are presented in Appendix A. We assume a solid crust with a fixed magnetic field, which is dipolar for the results presented in Section 3 and a mix of dipole and quadrupolar fields in Section 5. MPI and updated coordinates allow us to present an extended simulation domain and larger grid resolution such as 5000^2 relative to previous works.

2.3 Equation of state

In the outer envelope of the neutron star, matter has a composition of degenerate electron gas and strongly coulomb coupled ions. The pressure is dominated by the electron gas (Haensel et al. 2007). Plasma is degenerate for $\rho>10^3$ g cm^{-3} for typical HMXB hotspot temperatures of 2×10^7 K (Coburn et al. 2002). Thus, Fermi gas EOS for zero temperature gives a fair estimation of the pressure in the mound. Fermi gas is relativistic beyond a density range of 10^6-10^7 g cm^{-3}. The densities at the base of the accretion mound may reach values of $\rho\gtrsim10^8-10^9$ g cm^{-3}. Thus, to cover the wide density range in such mounds, a simple polytropic approximation for the EOS is insufficient. Hence, we use an empirical function that very closely approximates the pressure of a Fermi gas to an accuracy 1.8 per cent (Paczynski 1983; Mukherjee 2017). The Paczynski EOS and a detailed comparison with the often used polytropic asymptotic forms of the Fermi EOS are presented in Mukherjee (2017). The Paczynski EOS is formulated as

$$p=\frac{\pi}{3}\frac{m_e^4c^5}{h^3}\frac{(8/5)x_F^5}{\sqrt{1+(16/25)x_F^2}} \tag{12}$$

where

$$x_F=\frac{1}{m_ec}\left(\frac{3h^3}{8\pi\mu_em_p}\right)^{1/3}\rho^{1/3}.$$

$G(\rho)$ used in equation (5) for the Paczynski EOS is

$$G=\frac{m_ec^2}{8\mu_em_p}\left(\frac{(15/2)+(32/5)x_F^2}{\sqrt{1+(16/25)x_F^2}}\right). \tag{13}$$

We have assumed pure ionized helium matter ($\mu_e=2.0$) for all the mound simulations unless specified otherwise.

2.4 Boundary conditions

2.4.1 *Inner radial boundary $R=R_{\rm in}$*

The inner radial boundary is assumed to be a fixed dipole on the hard crust of the neutron star, which keeps the mound stable from interchange modes (Payne & Melatos 2004; Vigelius & Melatos 2008). However, in a realistic scenario, a mixture of accreted matter and neutron star matter at the inner boundary is expected to sink into the ocean and outer crust due to gravitational compression. However, such a sinking boundary condition (e.g. Wette et al. 2010) has not been directly implemented in this work and will be explored in the future. The impact of accretion on a pre-existing atmosphere has been partly addressed in Section 4.3, although the inner boundary is assumed to be fixed even in that subsection.

2.4.2 *Outer radial boundary $R = R_{\mathrm{out}}$*

As calculated in Payne & Melatos (2004), Greens function solution for the GS operator is given by

$$\psi(r',\theta') = \frac{\psi^{*}\sin^{2}\theta' R_{*}}{r'} + \sum_{\ell=1}^{\infty}\frac{\sin\theta' P_{\ell}^{1}(\cos\theta')}{2\ell(\ell+1)} \times \left(r'^{(-\ell)}\int_{0}^{\pi}\int_{R_{*}}^{r'} r^{\ell+1} Q(r,\ell) P_{\ell}^{1}(\cos\theta) K(\psi,r,\theta)\,\mathrm{d}r\,\mathrm{d}\theta + r'^{(\ell+1)} Q(r',\ell)\int_{0}^{\pi}\int_{r'}^{\infty} r^{-\ell} P_{\ell}^{1}(\cos\theta) K(\psi,r,\theta)\,\mathrm{d}r\,\mathrm{d}\theta \right). \tag{14}$$

where

$$Q(r,\ell) = \left(\left(\frac{R_{*}}{r}\right)^{2\ell+1} - 1 \right).$$

Here, $\psi^{*} = \frac{1}{2}B_{d}R_{*}^{2}$, where B_{d} is the dipolar magnetic field at the poles, and $K(\psi, r, \theta)$ is the source function from equation (9).

Using the Greens function formalism, we update the outer radial boundary value (R_{out}) at each iterative SOR step by utilizing the value of ψ at a radius R_{in} just above the maximum height r_c of the mound. ψ at the boundary is calculated from

$$\psi(R_{\mathrm{out}},\theta') = \sum_{\ell=1}^{\ell_{\max}} \left(\frac{(2\ell+1)P_{\ell}^{1}(\cos\theta')\sin\theta'}{2\ell(\ell+1)} \times \left(\frac{R_{\mathrm{in}}}{R_{\mathrm{out}}}\right)^{\ell} (1+(-1)^{\ell+1}) \times \int_{0}^{1}\frac{\psi(R_{\mathrm{in}},\cos\theta)P_{\ell}^{1}(\cos\theta)}{\sqrt{1-\cos^{2}\theta}}\,\mathrm{d}(\cos\theta) \right). \tag{15}$$

Derivation of this equation is presented in Section B1 (Appendix B). $\ell_{\max}$ has been chosen to be 33 for all simulations by several tests performed in Section B2 (Appendix B). R_{in} needs to be selected at a point in vacuum above the diamagnetic screening currents (Payne & Melatos 2004). The above boundary condition has been validated by a comparison with a greens function-based boundary condition involving volume terms described in Section B3 (Appendix B).

2.4.3 *Latitudinal boundaries*

At the magnetic pole (i.e. $\theta = 0^{0}$) it is assumed that $\psi = 0$. At the magnetic equator (i.e. $\theta = 90^{0}$), we assume a symmetric solution given by $\frac{\partial\psi}{\partial\cos\theta} = 0$.

2.5 Parameter space and profile function

We assume the values of the properties noted in Table 1 to be constant for all simulations. A near Eddington accretion rate ($L_{Edd} = \eta\dot{M}c^{2}$) where $\eta = 0.16$ is assumed to find some of the largest stable mound masses possible. The angular extent of the simulation is $\theta \in [0^{0}, 90^{0}]$ for a dipolar inner boundary while it is $\theta \in [0^{0}, 180^{0}]$ for a quadrudipolar case. Each GS solution is further characterized by the following parameters:

(i) Surface magnetic field strength B_d.
(ii) Maximum height of the mound r_c.
(iii) ζ = ratio of truncation radius (r_t) to Alfvén radius (R_A).
(iv) Truncation angle $\theta_t(\zeta, B_d, R_*, \dot{M}, M_*)$, as defined in equation (17).
(v) Form of the profile function $r_0(\psi, R_*, r_c, \theta_t)$ (shape of the density profile, e.g. equation 16).

The profile function ($r_0(\psi)$) defines the shape of the mound and the radial distribution of matter in the mound. Previously, various forms of this function have been explored to solve the GS equation (Hameury et al. 1983; Brown & Bildsten 1998; Mukherjee & Bhattacharya 2012; Mukherjee et al. 2013a; Mukherjee 2017). In all such cases, the outer angular edge of the mound corresponds to a truncation angle of θ_t, which has been determined by the inner edge of the accretion disc. In this work, we have primarily used the ring-shaped mound profile or the hollow mound profile (Mukherjee & Bhattacharya 2012; Mukherjee 2017) along with some other profiles. The ring-shaped mound profile is

$$r_0(\psi) = R_* + \frac{r_c}{0.25}\left(0.25 - \left(\frac{\psi}{\psi_a(\theta_t)} - 0.5\right)^{2}\right) \quad 0.0 \leq \psi \leq \psi^{*} \tag{16}$$

$r_0(\psi) - R_*$ is negative for $\psi > \psi_a$. Thus, ρ which is a function of $r_0(\psi) - r$ is defined to be zero for $\psi > \psi_a$. For $\psi > \psi_a$, though $\mathrm{d}r_0/\mathrm{d}\psi$ has some finite value, RHS term or source term $K(\psi, r, \theta)$ is zero due to zero ρ. Though an accretion profile depends on complex disc magnetosphere interaction where the matter penetrates through the magnetosphere (based on effective diffusivity) in non-axisymmetric 3D instabilities such as Rayleigh Taylor and Kelvin Helmholtz instabilities (Arons & Lea 1976a, b), such considerations require a complicated and non-axisymmetric analysis which is outside the scope of this work.

Ring-shaped mound profile requires two input parameters – maximum height (r_c) of the mound and the truncation angle (θ_t). The truncation angle (θ_t) is calculated from the accretion disc truncation radius (r_t) as

$$\theta_t = \sin^{-1}\left(\sqrt{\frac{R_*}{r_t}}\right). \tag{17}$$

We assume the truncation radius to be fraction of the classical Afvén radius (R_A) as $r_t = \zeta R_A$, where the Alfvén radius is given by (Psaltis & Chakrabarty 1999; Mukherjee et al. 2015; Mukherjee 2017)

$$R_A = 3.53\times 10^{3}\ \mathrm{km}\left(\frac{B_d}{2.0\times 10^{12}\ \mathrm{G}}\right)^{\frac{4}{7}}\left(\frac{R_*}{10\ \mathrm{km}}\right)^{\frac{12}{7}} \times \left(\frac{\dot{M}}{10^{-9}\ \mathrm{M}_{\odot}\ \mathrm{yr}^{-1}}\right)^{-\frac{2}{7}}\left(\frac{M_*}{1.4\ \mathrm{M}_{\odot}}\right)^{-\frac{1}{7}}. \tag{18}$$

As R_*, M_*, and $\dot{M}$ are fixed for all models, in this work θ_t primarily depends on B_d and ζ. We have performed simulations for different surface magnetic field strengths $B_d \in (10^{9}, 10^{10}, 10^{11}, 10^{12})$ G. Magnetohydrodynamic (MHD) simulations generally find the truncation radius to vary as $r_t = 0.5 - 1.0 R_A$ (Long, Romanova & Lovelace 2005; Bessolaz et al. 2008; Romanova, Kulkarni & Lovelace 2008; Zanni & Ferreira 2009; Kulkarni & Romanova 2013; Parfrey &

Tchekhovskoy 2017; Parfrey, Spitkovsky & Beloborodov 2017). For each B_d, we solve the GS equations for five different values of ζ viz. $\zeta \in (0.6, 0.7, 0.8, 0.9, 1.0)$, with $\zeta = 1$ corresponding to $r_t = R_A$ and hence $\theta_t = \theta_A$. Furthermore, for a given choice of ζ and B_d, various simulations have been performed for different mound heights (r_c) to scan a wide range of parameter space. In Sections 3.2, 4.1, last part of Sections 4.2.1, 4.3, and Appendix C2, θ_t is arbitrarily chosen to explore hypothetical maximal mass loading, and is not calculated from equation (17). In such cases, it has been explicitly specified that an arbitrary θ_t has been selected. The total mass of the mounds near both poles (M) is computed by integrating the density over all volume in the domain for all runs, with higher r_c, yielding larger mound masses.

3 DIPOLAR INNER BOUNDARY FOR RING-SHAPED MOUND PROFILE

This section presents results for a dipolar boundary at the neutron star surface and a multipolar CFB condition at the outer boundary along with a comparison of CFB to other boundary conditions. The results of GS solutions for a typical magnetically confined mound with a CFB are presented in Section 3.1. In Section 3.2, the new boundary condition and the effect of the boundary condition at the outer radial boundary have been discussed.

3.1 General description of GS solutions of mounds

To demonstrate the form of the final solutions using CFB, the results of a 5000 × 5000 simulation of an accretion mound with parameter values of $B_d = 10^9$ G, $\theta_t = \theta_A = 45.5^0$, $r_c = 4.7$ m, $M = 2.952 \times 10^{-13}\ \mathrm{M}_\odot$ are plotted in Fig. 1. The plot at the top of Fig. 1 is a density profile of the mound where the solid lines represent the magnetic field lines while the dashed lines are the dipolar field lines. The magnetic field lines are contours of ψ (placed equidistant in ψ) and thus in all the plots of the paper, the tangent to the lines represents the direction of the magnetic field but the density of the magnetic field lines is not equal to the magnetic field magnitude.

The ring-shaped mound profile pushes the magnetic field lines outwards. The magnetic field geometry is similar to the solutions presented before in spherical (Mukherjee 2017) and cylindrical coordinates (Mukherjee & Bhattacharya 2012). Inside the mound, B increases to $\sim 10^{11}$ G, two orders of magnitude larger than the starting magnitude of the dipole magnetic field at the base of the mound. Above the mound in vacuum, B increases near the two edges of the mound as the mound tends to stretch in both directions. The value of B is reduced right above the mound to accommodate the stretching. To quantify the deviation from the initial dipolar magnetic field, we present in the lower panel of Fig. 1 the colourmap of Y_{dip}, defined as

$$Y_{\mathrm{dip}}(r, \theta) = \frac{|B(r, \theta) - B_{\mathrm{dip}}(r, \theta)|}{B(r, \theta)}, \qquad (19)$$

where B is the magnitude of the magnetic field vector. For this example, we can see that B differs from the dipolar solution by 10 per cent–5 per cent for a height of 3–5 km above the neutron star surface. Maximum height above the neutron star surface till which $Y_{\mathrm{dip}}(r, \theta)$ has values 0.1 and 0.05 have been noted down in Table 2 for different magnetic fields and truncation angle $\theta_t = \theta_A$ for a given maximum mass allowed by our solutions (Appendix C). Low magnetic field pulsars have a larger deviation from the dipolar field than high magnetic field pulsars due to relatively higher θ_t values of the former's solutions. For the given range of magnetic fields, B

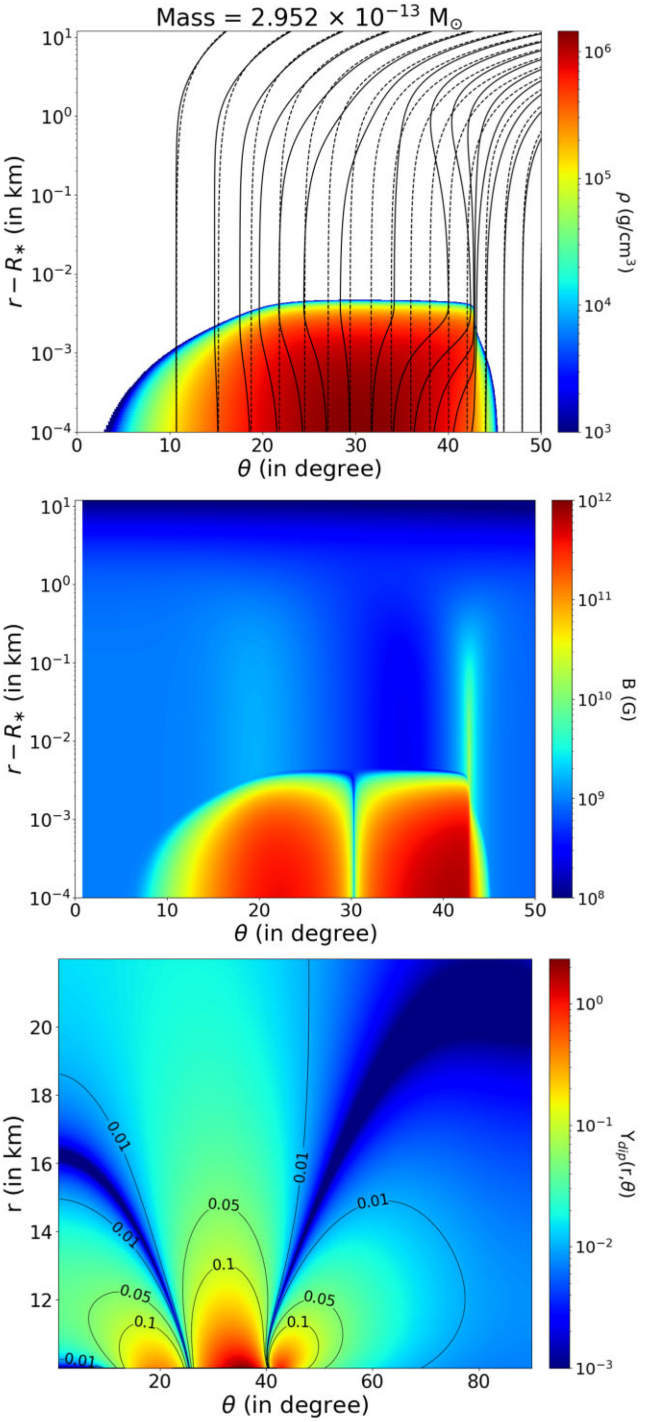

Figure 1. Plot of density profile and magnetic field lines (solid) for parameters $B_d = 10^9$ G, $\theta_t = 45.5^0$, $r_c = 4.7$ m, $M = 2.952 \times 10^{-13}\ \mathrm{M}_\odot$ (top), colourmap of magnetic field magnitude B (in Gauss) (middle) and colourmap of Y_{dip} (equation 19) (bottom). Dashed lines in the top figure are dipolar magnetic field lines. The accretion mound changes the magnetic field at the surface of the neutron star to a range of $10^8 - 10^{11}$ Gauss. Bottom plot has an extended θ range to show the deviation from the dipolar field in the whole simulation domain. There is a significant deviation of 10 per cent to 5 per cent from a dipolar solution till a height of 3−5 km above the neutron star surface due to an accretion mound.

Table 1. Name of the fixed properties and its values for the calculations performed are noted in this table.

Name	Value
Mass of the neutron star (M_*)	1.4 $M_\odot$
Radius of the neutron star (R_*)	10 km
Mass accretion rate ($\dot{M}$)	1.94×10^{-8} $M_\odot$ yr^{-1}
Outer radius of the simulation domain ($R_{\rm out}$)	22 km
$\ell_{\max}$ (Appendix B)	33

Table 2. The table lists results of GS solutions with different magnetic fields (first column) and truncation angle (second column). The maximum height ($h_{\max} = r - R_*$) where GS solution deviates by 5 per cent and 10 per cent from a dipolar field (defined by $Y_{\rm dip}(r, \theta)$ in equation 19) are presented in the third and fourth columns, respectively. This demonstrates the vertical extent of the non-dipolar distortion for different neutron star and mound parameters.

B_d (G)	θ_t	$h_{\max}$ (km) $\left(Y_{\rm dip} = 0.05\right)$	$h_{\max}$ (km) $\left(Y_{\rm dip} = 0.1\right)$
10^9	45.5^0	9.5	5.2
10^{10}	21.7^0	2.5	1.7
10^{11}	11.0^0	1.14	0.82
10^{12}	5.7^0	0.7	0.53

differs from the dipolar field by 5 per cent to heights ranging from 0.7 to 9.5 km. This has significant implications for expected radiation from accretion columns and its polarization (Becker & Wolff 2007; Caiazzo & Heyl 2021).

3.2 Effects on solution due to outer radial boundary

3.2.1 *Current free boundary condition v/s fixed boundary condition*

This subsection aims to highlight the change in the final solution due to the deployment of CFB at the outer radial boundary instead of a fixed dipole boundary. The dipolar boundary is fixed to the dipolar ψ value for B_d at the radius $R_{\rm out}$ i.e. $\psi^* \sin^2\theta(R_*/R_{\rm out})$. Fig. 2 represents the difference between a solution with CFB (solid lines) and a solution with fixed boundary condition (red dot–dashed lines) at the outer radial boundary (5000 × 5000 simulation). We have plotted the solutions in Fig. 2 for two cases:

(i) Case 1 (Fig. 2, top): *Physically motivated* $\theta_t = \theta_A$; $B_d = 10^9$ G, $\theta_t = 45.5^0$, $r_c = 5.5$ m, $M = 5.42 \times 10^{-13}$ $M_\odot$

(ii) Case 2 (Fig. 2, bottom): *Arbitrarily large* θ_t *for high* B_d *to set masses similar to solutions by* Priymak et al. (2011); $B_d = 10^{12}$ G, $\theta_t = 84.0^0$, $r_c = 103.1$ m, $M = 1.47 \times 10^{-8}$ $M_\odot$.

From Fig. 2, we can conclude that CFB compresses or reduces the size of the magnetosphere and thus shows a reduction in the dipole moment at the outer radii. The change from a fixed boundary is greater for mounds with larger mass, as apparent in the lower part of Fig. 2. The fixed boundary condition restricts the movement of the magnetic field lines. The confined mass for the solution of case 2 is qualitatively similar to the results of Priymak et al. (2011), obtained using an outflow boundary condition. However, such a boundary results in radial magnetic fields, similar to a monopole and is not physically motivated. Thus the newly proposed current-free boundary yields results similar to maximal burial obtained earlier, with better physically motivated boundary constraints. In more recent works, bootstrapping methods have been applied to estimate the reduced dipole moment and calculate the outer boundary accordingly (Rossetto et al. 2023). However, such a boundary restricts the large-scale fields to be dipolar in nature, preventing free evolution due to deformations at the base. The CFB gives magnetic field lines more freedom to move while also maintaining the value of multipole moments in vacuum.

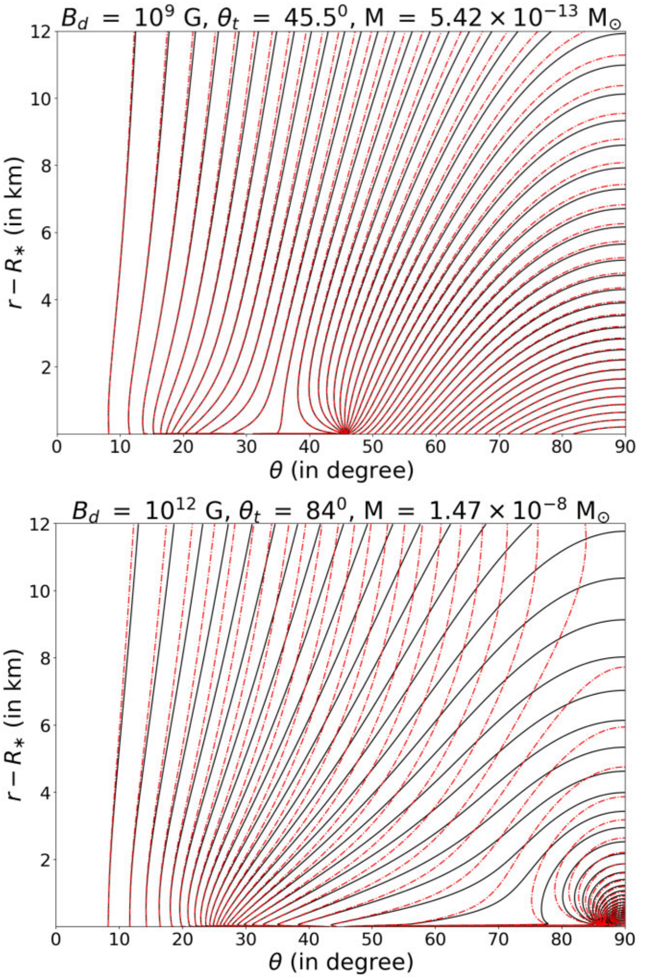
B_d = 10^9 G, θ_t = 45.5^0, M = 5.42×10^{-13} $M_\odot$

B_d = 10^{12} G, θ_t = 84^0, M = 1.47×10^{-8} $M_\odot$

Figure 2. Plots of magnetic field lines for fixed dipole condition (red dash–dotted lines) and CFB (black solid lines) at the outer radial boundary for case 1: $B_d = 10^9$ G, $\theta_t = 45.5^0$, $r_c = 5.5$ m, $M = 5.42 \times 10^{-13}$ $M_\odot$ (top) and case 2: $B_d = 10^{12}$ G, $\theta_t = 84.0^0$, $r_c = 103.1$ m, $M = 1.47 \times 10^{-8}$ $M_\odot$ (bottom). Magnetosphere gets compressed as dipole moment is lowered due to the accretion mound. Solutions for a larger mass (due to a high B_d and high θ_t) shows a larger deviation between the CFB and fixed dipole boundary condition.

3.2.2 *Effect of outer radius of simulation domain*

This subsection aims to highlight the effect of changing the value of the outer boundary of the solution domain on different boundary conditions. The accretion mound solution for case 2 from the previous Section 3.2.1 has been used to make these comparisons, as it denotes solutions with some of the largest mound masses and hence significant deviations from a dipolar magnetic field. In Fig. 3, we present solutions with two different choices of the outer radius of the compute domain for the GS solver: (a) $R_{\rm out} - R_* = 2$ km (solid lines) and (b) $R_{\rm out} - R_* = 12$ km (dash–dotted lines). The panels denote solutions with three different boundary conditions for the outer boundary: (a) fixed boundary in the upper panel, (b) an

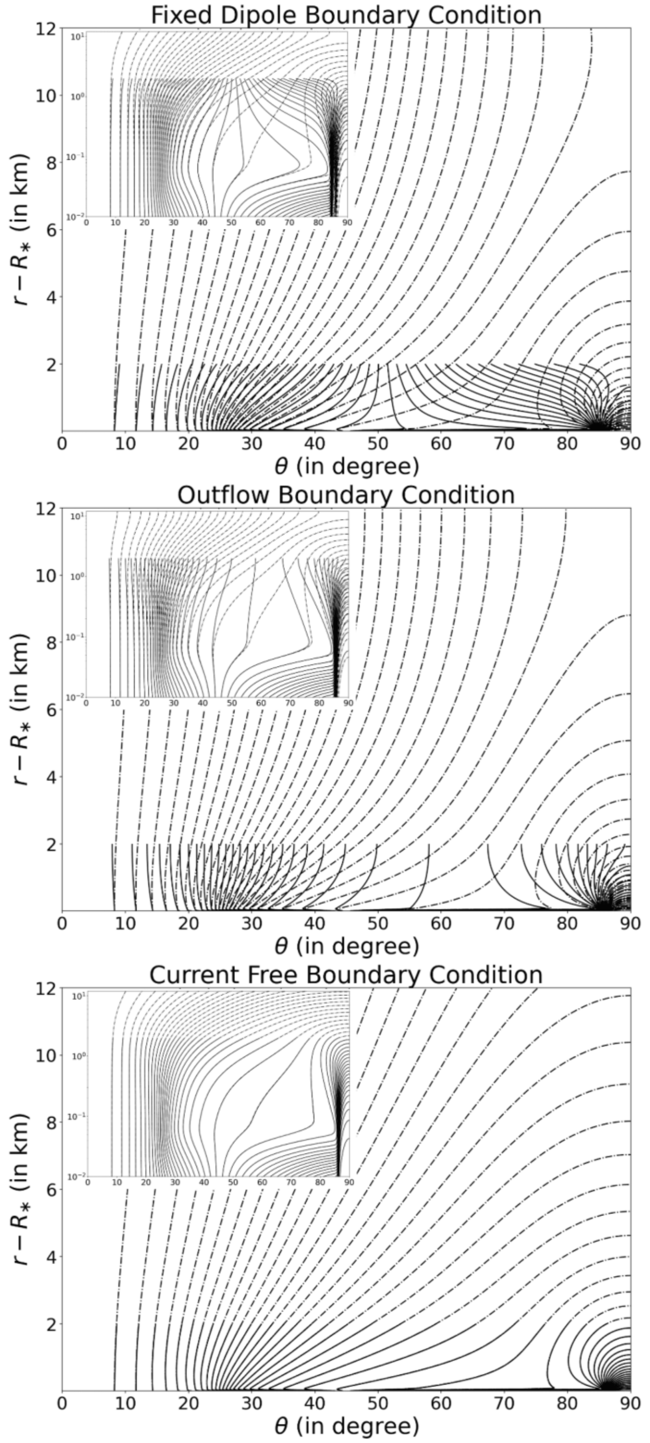

Figure 3. Plots of magnetic field lines for a small radial domain 2 km (solid lines) and a large radial domain 12 km (dash–dotted lines) with a fixed dipole boundary condition (top), outflow boundary condition (middle), and CFB (bottom) at the outer radial boundary for case 2 in Section 3.2.1. The inset plots show the same plots in logarithmic scale. Magnetic field line solutions for CFB seems to be independent of the choice of outer radius of the domain unlike the solutions for outflow boundary condition and fixed dipole boundary condition.

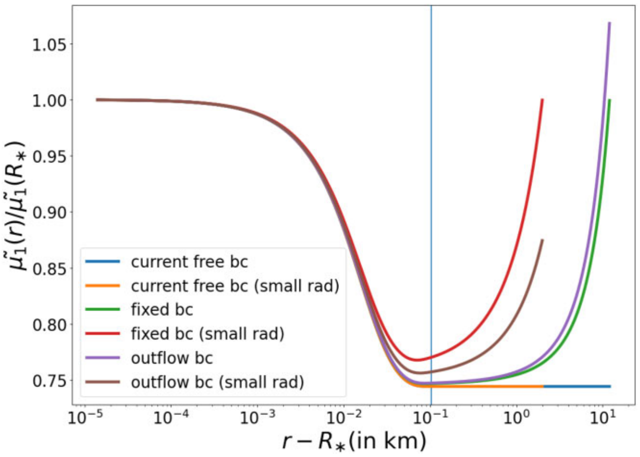

Figure 4. Normalized dipole moment at a radius above the neutron star relative to the normalized dipole moment at the surface of the neutron star (equation 20) plotted for solutions with three boundary conditions and two different simulation domains i.e. for six cases. Vertical line is the maximum height r_c of the mound. Dipole moment for the CFB condition solutions are constant in vacuum irrespective of the extent of the radial domain unlike the dipole moments for the other two boundary conditions.

outflow condition ($\frac{\partial \psi}{\partial y} = 0$) or a free boundary in the middle panel, and (c) the lower panel shows a solution with the new CFB. All solution domains with two different outer boundaries have the same grid structure up to the $R_{\text{out}} - R_* = 2$ km.

For both the fixed and the outflow boundaries, the solutions for the smaller compute domains differ significantly from those with larger R_{out}. This implies that the nature of the solutions depend on the choice of extent of the compute domain as larger deformations of field lines are supported in extended domains. Unlike the fixed and the outflow boundaries, solutions with a multipolar boundary for the two R_{out} are seen to overlap seamlessly. The change in the solutions with a multipolar boundary due the outer boundary are less than 0.01 per cent, unlike the solutions with fixed and outflow boundaries. However, to achieve the desired accuracy, solutions with smaller R_{out} require a larger number of multipole moments (equation 15). This inference has been established with a test in Appendix B2.3.

Thus, a CFB can be used to find the solution with sufficient accuracy for a smaller outer radial domain, allowing for higher resolution with limited computational resources.

The normalized ℓth magnetic multipole moment of the magnetosphere can defined as (Suvorov & Melatos 2020; Fujisawa et al. 2022, and references therein)

$$\tilde{\mu_\ell}(r) = r \int_0^\pi \psi(r, \theta) P_\ell^1(\cos\theta)\, \mathrm{d}\theta. \tag{20}$$

The normalized dipole moment at any radius relative to the normalized dipole moment at the surface of the neutron star (equation 20; $\ell = 1$) has been plotted for the above solutions in Fig. 4 as a function of height above the surface of the neutron star. The vertical line in Fig. 4 is the r_c (maximum height) of the mound. CFB solution for the smaller radial domain (orange curve) overlaps the CFB solution for the larger radial domain (blue curve) unlike the dipole moment ratios for the fixed boundary and outflow boundary condition. Dipole moment ratios of the larger domain solutions for the fixed (green curve) and outflow (purple) boundary conditions resemble the dipole moment ratios of the CFB solutions upto a particular height above r_c.

However, the dipole moment ratios of the smaller domain solutions for the fixed (red curve) and outflow (brown) boundary conditions deviate from the CFB dipole moment ratios even below r_c. This shows that as the radial extent of the compute domain increases, the dipole moment ratio of a different boundary condition solution tends towards the dipole moment ratios of a CFB solution. This validates the chosen CFB condition, since as the radial extent of the compute domain increases, the effect of the outer radial boundary condition on the solution reduces.

The ratio of normalized dipole moments for a fixed boundary approach 1.0 at the outer radius as expected, but the dipole moment ratios for the outflow boundary condition behave in a manner different from the solutions found by Priymak et al. (2011) and Suvorov & Melatos (2020). This could be due to the choice of the coordinates, as we assign an outflow boundary condition for our logarithmic radial coordinate, while the above-mentioned authors assign outflow boundary condition for the radial coordinate.

4 SOLUTIONS FOR LARGE CONFINED MASSES

One of the primary science goals in this domain is to understand how much mass can be contained by a mound for a given surface magnetic field (B_d) and angular extent (θ_t). Large mound masses are expected to result in stronger field reduction at the outer radius (field burial) and higher mass ellipticities, which are of strong interest for searches of CGWs (Bonazzola & Gourgoulhon 1996). In previous studies (such as Payne & Melatos 2004; Priymak et al. 2011; Mukherjee & Bhattacharya 2012), the maximum mass was limited by the appearance of closed field lines forming magnetic bubbles inside the solution domain, resulting in non-convergence of the GS iterations. In the first subsection, we show the results for the $1/\cosh$ profile used by Fujisawa et al. (2022). In the final two subsections, we investigate the nature of GS solutions for a physically motivated ring-shaped mound profile for different mound heights (and hence mass) to explore the appearance of a maximum mass, if any.

4.1 Filled mound with exponential decay beyond ψ_a

In the past, several authors have modelled mounds to be not strictly confined to a chosen θ_t, which would be expected in accreting systems with a well-defined inner radius (Mukherjee & Bhattacharya 2012; Mukherjee 2017). Instead, often an exponentially decaying profile function has been chosen (Payne & Melatos 2004; Priymak et al. 2011, 2014; Fujisawa et al. 2022). Such a profile results in significant mass loading to field lines beyond the $\theta(\psi_a)$ latitude, extending up to the equator (Mukherjee 2017). During a given accretion episode, such extended mass distribution is not possible for mass loaded field lines from an accretion disc with a finite inner edge, translating to a strict cut-off latitudinal angle (θ_t as in equation 17). None the less, an extended mass distribution may be used to motivate long-term accretion based confinement of matter. It is possible that during accretion, matter spreads out of confinement through reconfiguration of magnetic fields by ideal or resistive instabilities (Vigelius & Melatos 2009b; Suvorov & Melatos 2019; Kulsrud & Sunyaev 2020). Thus, the accretion mound might reconfigure to a larger size. To model such mounds and compare with earlier results, we perform GS solutions with a profile given by Fujisawa et al. (2022):

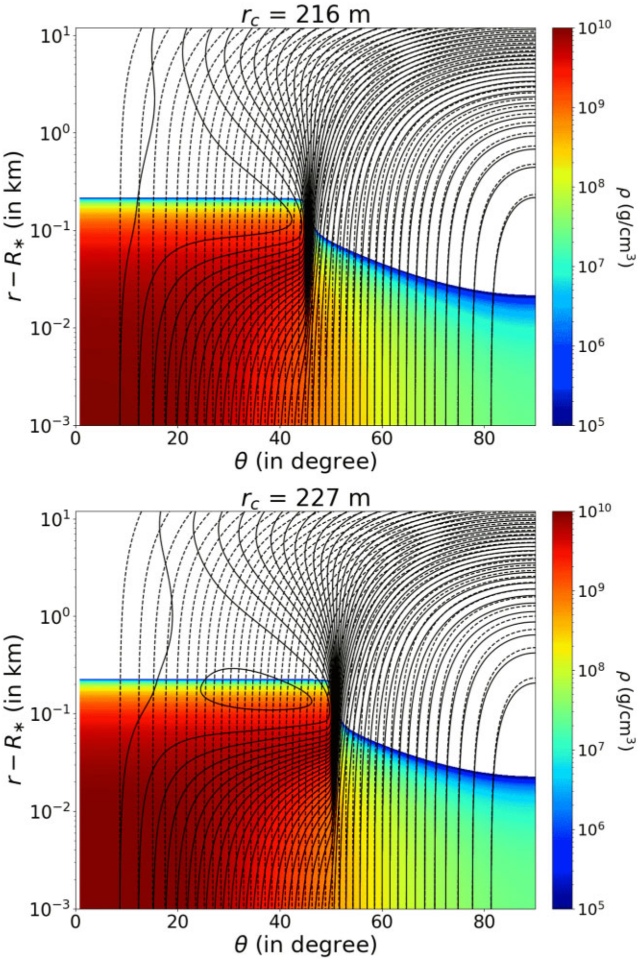

Figure 5. Density profiles and magnetic field lines (solid) for the $1/\cosh$ profile for $r_c = 216$ m (top) and $r_c = 227$ m (bottom). These solutions are calculated for a $B_d = 10^{12.5}$ G. Dashed lines are the undistorted dipolar magnetic field lines. Masses with an order of 10^{-8} $M_\odot$ can be simulated with this profile. Closed Magnetic loops (bottom plot) are detected in the solutions beyond a certain mass.

$$r_0(\psi) = R_* + \frac{r_c}{\cosh \frac{\psi}{\psi_a}}, \tag{21}$$

Fig. 5 shows an accretion mound with this profile (resolution 5000 × 5000) for parameter $\theta_t = 35.27^0$ and two values of r_c. The top plot in Fig. 5 has a single mound with a total mass of 4.23×10^{-8} $M_\odot$, with a mass of 1.43×10^{-9} $M_\odot$ beyond ψ_a. Accretion mounds of mass 10^{-8}–10^{-7} $M_\odot$ can be set with this profile for a high magnetic field of $10^{12.5}$ G (assumed by Priymak et al. 2011) before closed magnetic loops appear in the solution. Such closed magnetic loops have also been reported in several earlier works (Hameury et al. 1983; Payne & Melatos 2004; Priymak et al. 2011; Mukherjee & Bhattacharya 2012). These closed loops have been identified to arise due to the inherent susceptibility of the bent field lines to MHD instabilities, confirmed in dynamic simulations (Payne & Melatos 2007; Mukherjee et al. 2013a). Closed magnetic loops do not appear in the ring-shaped mound profiles unless the resolution is low and the solution is found from a perturbed guess (Fig. C3, Appendix Section C2). This likely results from the additional freedom of the field lines to bend towards the polar regions, which

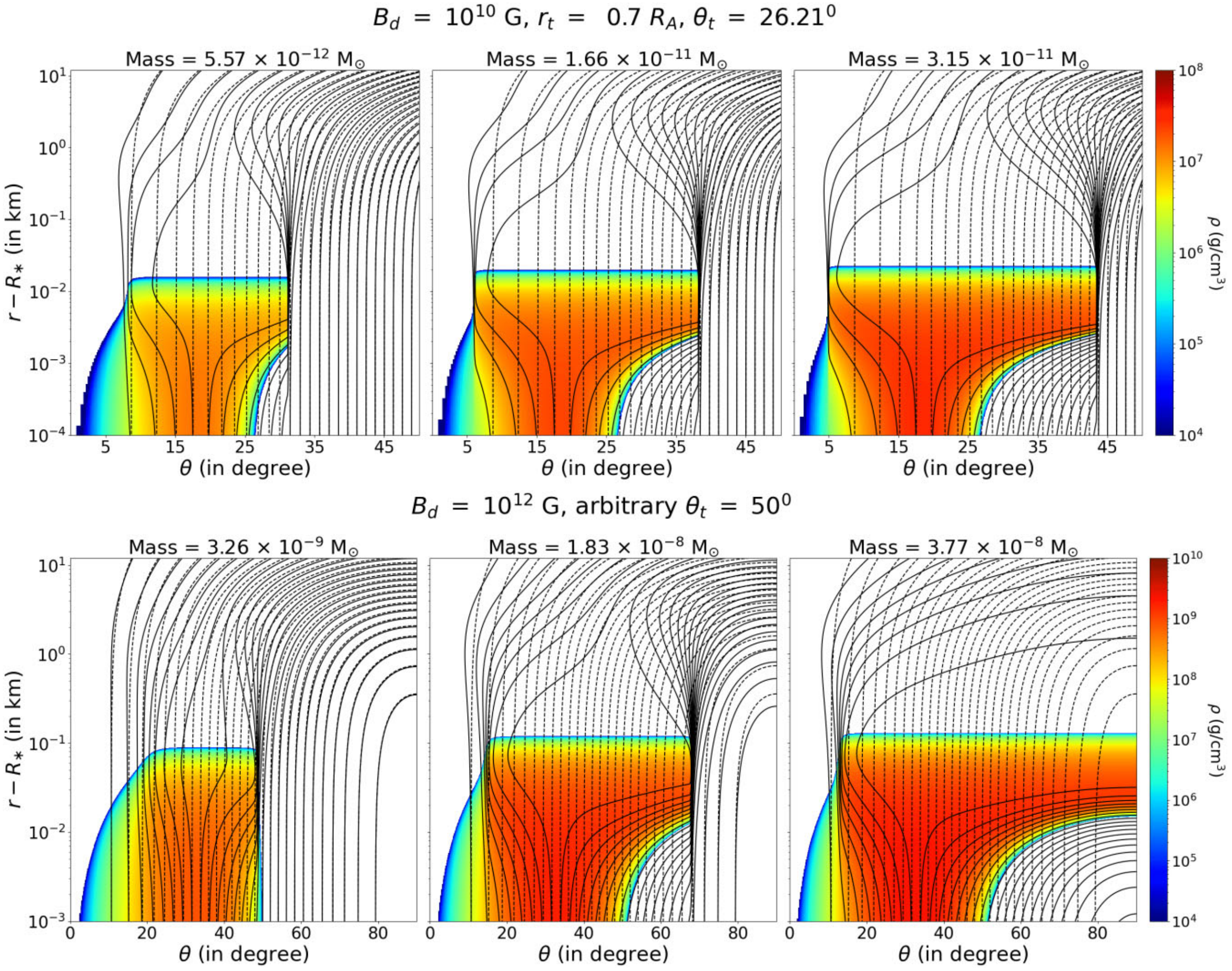

Figure 6. Density profiles and magnetic field lines (solid) for the ring-shaped mound profile for parameters $B_d = 10^{10}$ G, $r_t = 0.7R_A$, $\theta_t = 26.21^0$ (top plot) and parameters $B_d = 10^{12}$ G, arbitrary $\theta_t = 50^0$ (bottom plot). The top plot x-axis has a θ range of 0^0–50^0, while the bottom plot x-axis has a θ range of 0^0–90^0. Also, the colourbars have different ranges for the top and bottom plots. Both the top and bottom plots have resolution 5000×5000. r_c is increased and thus mass increases from top left to right and the same for the bottom plot. Dashed lines are the undistorted dipolar magnetic field lines. Mounds for the top plot with a physically motivated θ_t spread towards the equator, but the NMM is not evolved till the equator. Mounds for the bottom plot with an arbitrary θ_t spread towards the equator and the mounds are evolved till the equator. It must also be pointed out that the sequentially spreading solutions have a different $\mathrm{d}M/\mathrm{d}\psi$.

would otherwise have led to more severe distortions, as observed in filled mounds.

Thus, this profile is limited to a maximum mass above which closed loops related to magnetic field geometry appear in the solutions. Due to this limitation, this profile does not continue to spread without closed magnetic loops with increasing mass like the ring-shaped mound profile as discussed in the next subsection.

4.2 Ring-shaped mound

In this subsection, we outline the behaviour of GS solutions on increased mass loading for the physically motivated ring-shaped mound profile and describe different properties of the mound for this profile.

4.2.1 Latitudinal spreading of matter

The mass of the mound for the ring-shaped mound profile could be increased by increasing the angular extent of the mound (θ_t) and maximum mound height (r_c). For mound profiles modelled to be created from accretion episodes, θ_t is expected to be determined by the inner edge of the accretion disc, which is related to the Alfvén radius as $r_t = \zeta R_A$, as described in the Section 2.5. However, in this subsection and some of the other subsections, solutions have also been calculated for an arbitrary θ_t to explore larger masses. Such solutions present hypothetical large mass loading, beyond the confines of a single accretion episode, as described in the earlier subsection (Section 4.1). Once θ_t is fixed, for a particular B_d and θ_t, an increase in the height (r_c) of the mound leads to a higher confined accreted mass and larger magnetic field deformation.

This study finds that with an increase in confined mass, the ring-shaped mound spreads latitudinally both towards the pole and the equator. Two examples of such spreading solutions are presented in Fig. 6, where we see that the density profile has extended up to an angle greater than θ_t. A sequence of solutions with increasing r_c has been calculated and plotted for two cases: a physically motivated θ_t ($r_t = \zeta R_A$) and an arbitrary value of θ_t (similar motivation to case 2 in Section 3.2.1). We have calculated solutions till a maximum mass beyond which the uniqueness of solutions cannot be established and this maximum mass is limited by resolution. We call this the numerical maximum mass (NMM). The procedure for finding the NMM for a particular B_d and θ_t and the dependence of the NMM on resolution has been described for a case in Appendix C. From Fig. 6, we can see that the magnetic field lines have a limited poleward spread and an extensive equator-ward spread that successively increases with mass. A higher equator-ward spread reduces the dipole moment above the mound as discussed later in Section 4.2.4. Such an equator-ward spread was also found by Payne & Melatos (2004), Priymak et al. (2011), and Fujisawa et al. (2022). However, all such previous models populated the matter on all the magnetic field lines from the pole to the equator. Such spreading becomes more explicitly demonstrated in the current results, where the matter distribution is shown to have higher angular extent than the foot point of the last matter loaded field line, given the choice of the truncation angle (θ_t). These results were found for all the mounds calculated in this paper. For physically motivated θ_t ranges, the latitudinal spread was limited to an angle less than 90^0 (before the equator) due to NMM constraints as described in Section 4.2.3. For an arbitrary θ_t, the mound has a latitudinal spread till the equator as described in Section 4.2.4.

One must note that the mass beyond θ_t with a height of 22.63 meters in the upper part and rightmost plot of Fig. 6 is supported against gravity by a vacuum region of height three meters (the y-axis of Fig. 6 is in log scale) with strong B_θ fields. Such solutions may not be stable and their dynamical stability should be verified.

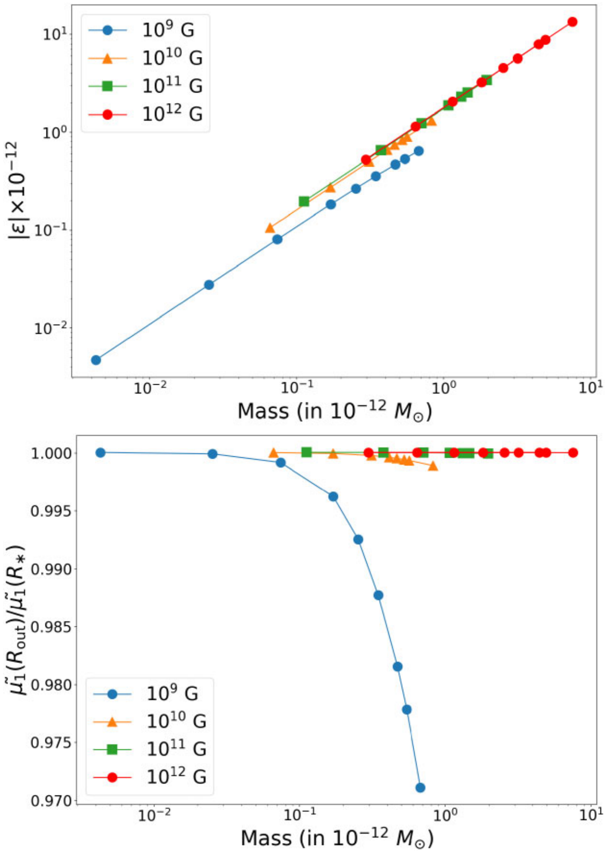

Figure 7. Top plot has absolute mass ellipticity of the 2 mounds on the y-axis and mass of the two mounds on the x-axis for four values of B_d. Ellipticity is proportional to the accreted mass. Bottom plot has normalized dipole moment at the outer radius relative to its value at the neutron star surface varying with the accreted mass of the two mounds for four values of B_d. See Section 4.2.2 for further description.

4.2.2 *Ellipticity and relative dipole moment behaviour for $r_t = R_A$*

The results in this subsection are for simulations with grid size of 10000 × 10000, except for cases with $B_d = 10^{12}$ G, where low values of $\theta_t (\lesssim 5.7^0)$, necessitates higher resolution (12000 × 12000). θ_A has been calculated assuming the accretion disc to be truncated at R_A (equation 18). Although we have run a suite of simulations with different mound masses (by varying r_c), the solutions have not been calculated until a maximum mass (NMM) due to the compute intensive nature of the exercise. However, the results depict the general trend of the variation of the derived parameters such as mass ellipticity and normalized relative outer dipole moment (equation 20) with mass. We define ellipticity ϵ (Priymak et al. 2011; Fujisawa et al. 2022) as

$$\epsilon = \frac{I_{zz} - I_{xx}}{I_0}, \tag{22}$$

where $I_0 = 1.11 \times 10^{45}$ g cm^{-2} is the moment of inertia of a spherically symmetric neutron star. I_{jj} is the moment of inertia tensor about the j coordinate axis. Here, Z-axis is the magnetic axis. The mass and absolute ellipticity for four different B_d are plotted in the top plot of Fig. 7. As found in previous works (Priymak et al. 2011; Suvorov & Melatos 2020; Fujisawa et al. 2022; Rossetto et al. 2025), the absolute ellipticity of our solutions is proportional to the accreted mass. Also, as shown in the bottom plot of Fig. 7, the value of $\tilde{\mu_1}(R_{\rm out})/\tilde{\mu_1}(R_*)$ (equation 20) decreases with increasing accreted mass.

4.2.3 *Results for $r_t = \zeta R_A$*

To find the impact of mound masses on different properties of such systems such as mass ellipticities, efficiency of field burial and truncation angles θ_t, we have performed a suite of GS solutions. Numerical simulations of magnetized accretion on to neutron stars (such as Long et al. 2005; Bessolaz et al. 2008; Romanova et al. 2008; Zanni & Ferreira 2009; Kulkarni & Romanova 2013; Parfrey et al. 2017; Parfrey & Tchekhovskoy 2017) predict the truncation radius of the accretion disc to be smaller than the traditional Alfvén radius ($r_t \sim 0.5$–$1.0 R_A$). We have thus varied r_t in the range $0.6 - 1.0\ R_A$, to obtain different values of θ_t for a given B_d and repeated the activity for four different magnetic fields ($B_d \in (10^9, 10^{10}, 10^{11}, 10^{12})$ G), for a total of 20 solutions. For each of the 20 solutions, r_c is increased to get a higher confined mass. Although we are limited by numerical diffusion, we chose to perform all simulations with the same resolution 5000 × 5000 to draw a generic set of conclusions for the physical parameters of interest. An example of the density profiles and magnetic field lines of one of these results are plotted in the upper part of Fig. 6. The mass and dipole moments for all the results are depicted in Figs 8 and 9.

In Figs 8 and 9, the coloured points correspond to the maximum mass allowed by our simulations (NMM) (Appendix C). The grey points in these figures are the other solutions with a lower r_c. The four figures plotted are for four values of B_d. For each B_d figure, accreted mass and $\tilde{\mu_1}(R_{\rm out})/\tilde{\mu_1}(R_*)$ are plotted against the five values of θ_t in Figs 8 and 9, respectively. Most of these solutions spread towards the equator with matter going beyond θ_t as in Fig. 6. The horizontal bar in Figs 8 and 9 shows the extent of the angular spread of the mound beyond θ_t. Here are the primary results:

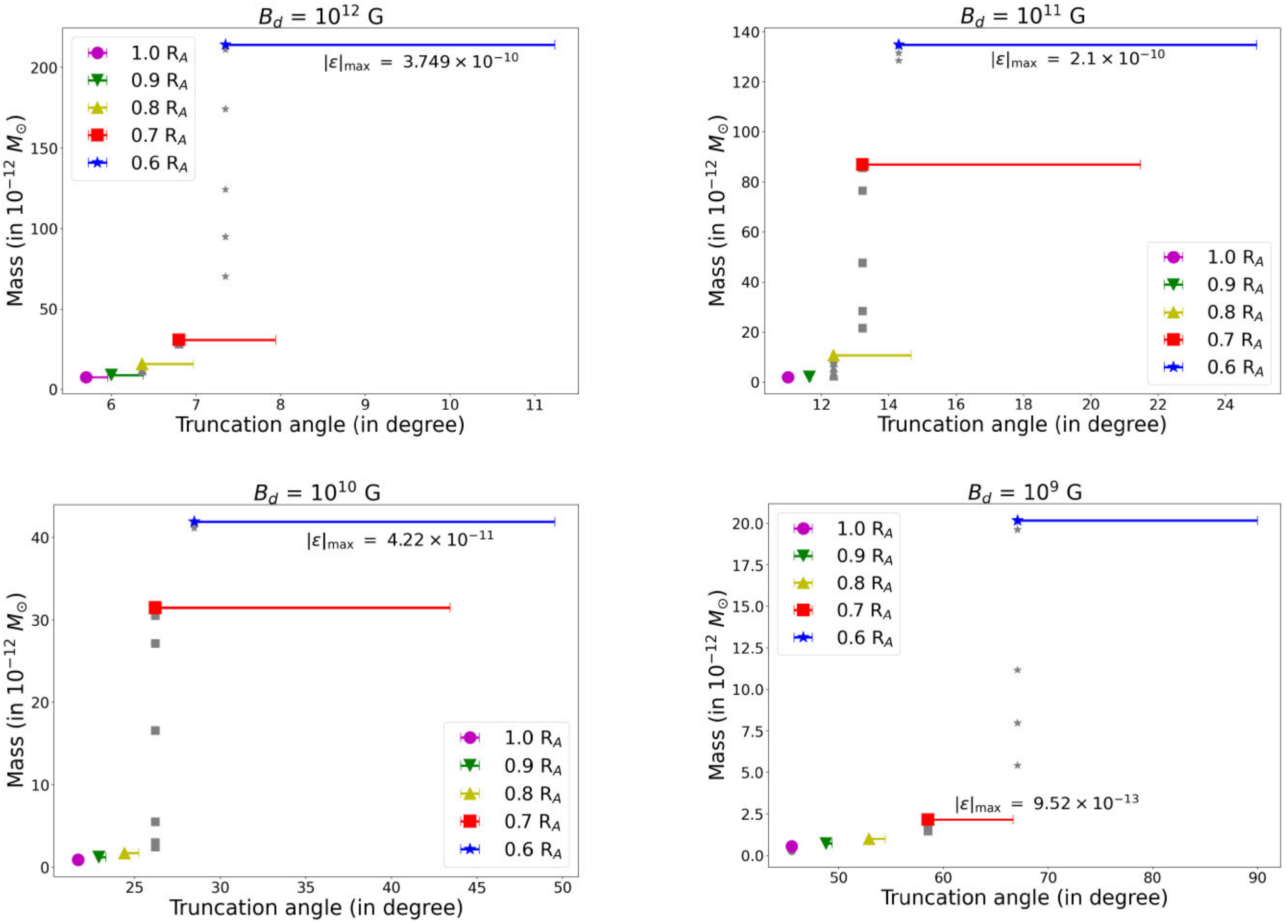

Figure 8. Plot of mass (in 10^{-12} $M_\odot$) for five different possible truncation angles (θ_t) made for four surface magnetic field strengths (B_d). The coloured symbols indicate the maximum mass (NMM) set by this simulation for a respective θ_t, while the grey symbols are the solutions for a lower height. The errorbars show the latitudinal angular spread of matter beyond θ_t. See Section 4.2.3 for further description.

(i) Higher mass of the mounds could be accreted and confined for a higher B_d. For a particular B_d, Fig. 8 clearly shows that if θ_t is higher, the angular extent of matter is greater (both θ_t and the equator-ward spread is high), and thus the amount of accreted mass is higher.

(ii) Fig. 8 also shows the maximum absolute mass ellipticity obtained by our calculations for the four magnetic fields. For the four magnetic fields ($10^9, 10^{10}, 10^{11}, 10^{12}$) G, the maximum absolute ellipticities are $9.52 \times 10^{-13}, 4.22 \times 10^{-11}, 2.1 \times 10^{-10}, 3.75 \times 10^{-10}$, respectively. The value of these ellipticities serves as a lower limit (since most of the mounds have a further chance of spreading). However, the impact of MHD instabilities has not been considered. There could also be a contribution to the ellipticity purely due to the presence of a magnetic field (Nazari & Roshan 2020; Rossetto et al. 2025). Rossetto et al. (2025) found the absolute magnetic ellipticity to be six orders lower than the absolute mass ellipticity. In this paper, the maximum absolute magnetic ellipticity for the four magnetic fields ($10^9, 10^{10}, 10^{11}, 10^{12}$) G were found to be $2.43 \times 10^{-17}, 9.32 \times 10^{-16}, 10^{-14}, 5.6 \times 10^{-14}$, respectively, which is approximately four orders lower than the maximum absolute mass ellipticity.

(iii) Fig. 9 shows the value of $\tilde{\mu_1}(R_{\rm out})/\tilde{\mu_1}(R_*)$ for all solutions. For a particular B_d, since larger masses lead to lower dipole moments at the outer radius, an increase in the θ_t values decreases the values of $\tilde{\mu_1}(R_{\rm out})/\tilde{\mu_1}(R_*)$. The solution with $B_d = 10^9$ G, $\zeta = 0.6$ has its matter extended till the equator, and we find the highest field burial for this solution with a value of $\tilde{\mu_1}(R_{\rm out})/\tilde{\mu_1}(R_*) = 0.627$.

(iv) Change in higher moments ($\ell > 1$) is insignificant for our solutions, except for the low field 10^9 G, $\zeta = 0.6$ solution, where the relative octupole moment is about 0.12.

The latitudinal spreading by the ring-shaped mound profile is the true depiction of field burial predicted before through semi-analytic studies (Hameury et al. 1983; Melatos & Phinney 2001). We have a solution with a latitudinal spread till the equator only for the case $B_d = 10^9$ G, $\zeta = 0.6$. For all the other cases, we have not calculated solutions that have a latitudinal spread till the equator due to computational constraints. In a future work, we will attempt to find the latitudinal spreading of mounds with θ_t near the poles, spreading from the pole to the equator, to explore the highest field burial achievable.

4.2.4 Results for arbitrary θ_t

Though θ_t for a mound with $B_d = 10^{12}$ G is as low as $5.7 - 7.3$ degree if constrained to $\theta_t = \theta_A$, for the purpose of demonstration and to have a high θ resolution near θ_t we simulate accretion mounds for an arbitrary $\theta_t = 50^0$. As shown in the lower part of Fig. 6, the mound starts to spread towards the equator, but the mass beyond $\theta > \theta_t$ is completely supported by the vacuum magnetic field against

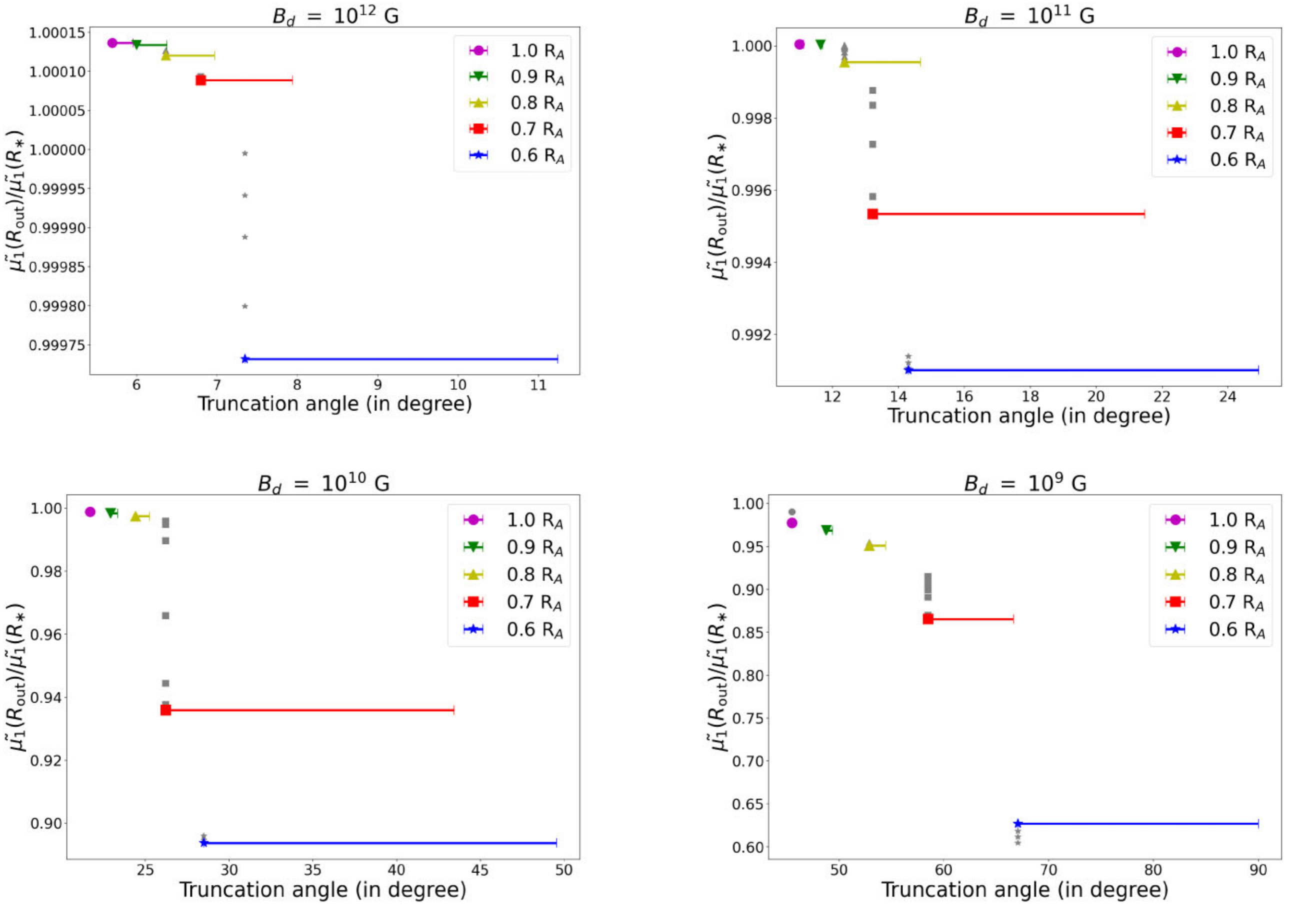

Figure 9. Plot of normalized dipole moment at the outer radius relative to its value at the NS surface for five different truncation angles (θ_t) made for four surface magnetic field strengths (B_d). The coloured symbols indicate the maximum mass (NMM) set by this simulation for a respective θ_t, while the grey symbols are the solutions for a lower mass. Errorbars show the equator-ward angular spread of matter beyond θ_t. See Section 4.2.3 for further description.

gravity. Before the mound spreads towards the equator as shown in the lower part of Fig. 6, some resistive instabilities (Vigelius & Melatos 2009b; Suvorov & Melatos 2019; Kulsrud & Sunyaev 2020) could result in diffusion of matter near θ_t, where the magnetic field lines bunch together. This might change θ_t and the magnetic geometry, thus automatically invalidating the solutions given in Fig. 6. Even cumulative accretion episodes could change θ_t. In addition, the solutions shown in the lower part of Fig. 6 increase in mass sequentially, but we should understand that they do not come from sequential accreting episodes, since they have a different $\mathrm{d}M/\mathrm{d}\psi$.

Ellipticity and change in multipole moments of these solutions are plotted in Fig. 10. The topmost plot of Fig. 10 shows that there is a turnover in ellipticity after a certain mass, as the mound spreads towards the equator, unlike the ellipticity in Fig. 7 which is not evolved till equator. Finally, as the mound reaches the equator, the ellipticity does not change appreciably. The middle plot of Fig. 10 shows that the dipole moment keeps reducing as the mound mass increases, and the mound stretches the magnetic field lines and matter towards the equator. As the mound reaches the equator, the dipole moment remains more or less constant. The ratio of normalized dipole moments (except the last point) is found to have the behaviour

$$\frac{\tilde{\mu_1}(R_{\rm out})}{\tilde{\mu_1}(R_*)} = 0.994 - \left(0.00386 \times \left(\frac{\rm Mass}{10^{-9}\mathrm{M}_\odot}\right)^{1.376}\right). \quad (23)$$

The bottom plot of Fig. 10 shows that the octupole moment initially decreases and then increases as the mass keeps on increasing. When the mound reaches the equator, octupole moment remains the same. $\ell = 5$ and $\ell = 7$ moments do not show a significant change as the mass of the mound increases.

4.3 Ring-shaped mound on a neutron star atmosphere and ocean

The neutron star surface is expected to have a liquid ocean and gas layer over the solid crust with a height ranging from ~ 3 to 1700 cm (Nättilä et al. 2024). Current models of accretion mounds obtained using the GS solver do not take into consideration a pre-existing ocean and atmosphere. Here, we try to construct a profile by considering a mound mixed with and sunk into the neutron star ocean and atmosphere. This is similar to the profile suggested by Melatos & Phinney (2001) but with significant changes.

A pre-existing current free neutron star ocean and atmosphere threaded with an initial dipolar magnetic field which is fixed at a radius R_b is assumed here. The matter falls on the neutron star ocean through a surface angular range of $\theta_\ell \leq \theta \leq \theta_t$ confined by the magnetic field lines with θ_ℓ constrained by the light cylinder and θ_t by the accretion disc inner radius. Matter mixes with the ocean and atmosphere, modifying the density profile and magnetic geometry above R_b in the range $\psi_{\rm ap} \leq \psi \leq \psi_a$ and thus forms the accretion mound. It is assumed that beyond this range, the envelope is current free even after accretion and the height of the envelope above the inner boundary of the domain (R_b) is fixed. Thus, for this

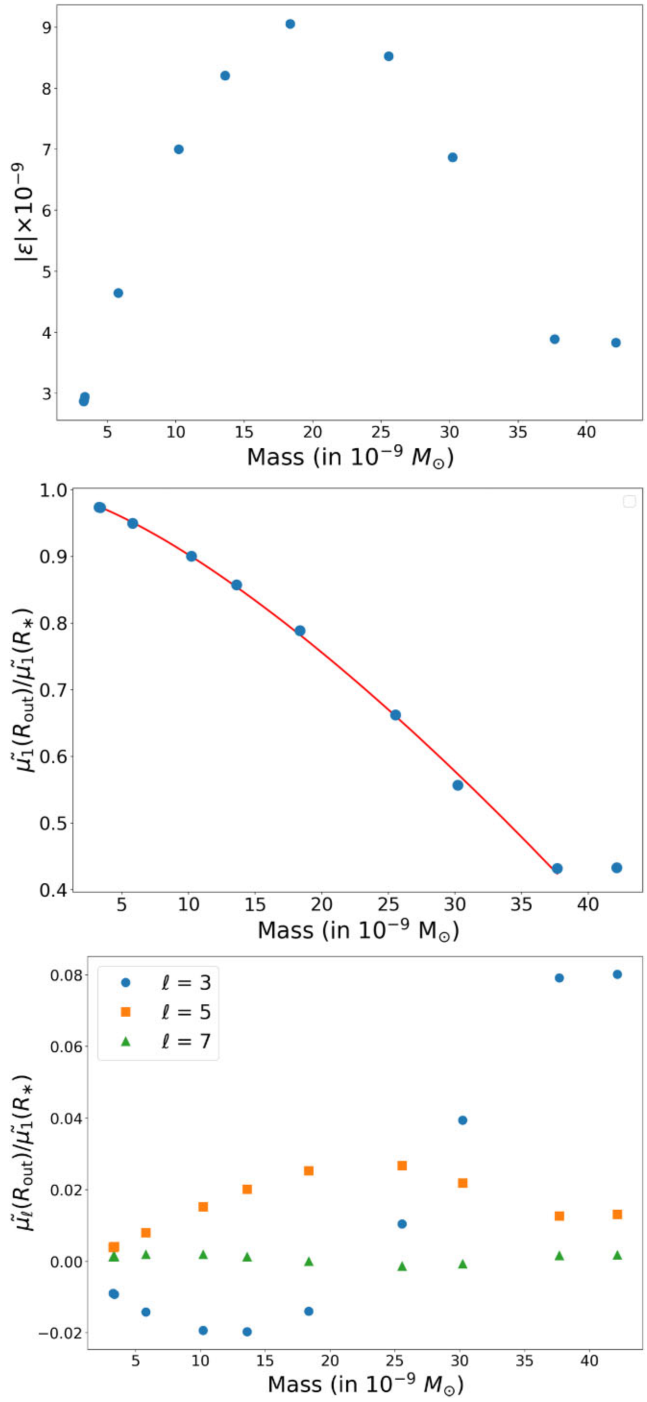

Figure 10. The parameters for all the three plots are $B_d = 10^{12}$ G and an arbitrary $\theta_t = 50^0$. The topmost plot has shown absolute ellipticity as a function of mass. The middle plot has shown normalized dipole moment at the outer radius relative to its value at the neutron star surface as a function of mass. Blue points in this plot (except the last point) is fitted to the function $y = ax^b + k$ with a red line. The bottom plot has shown higher normalized multipole moments at the outer radius relative to dipole moment value at the neutron star surface as a function of mass. See Section 4.2.4 for further description.

profile, the inner boundary (R_b) is not the surface of the neutron star, but it is a radial limit above which the mass loading profile per magnetic field line ($dM/d\psi$) of the neutron star has been modified by accretion, and the dipolar magnetic field is fixed at this radius. This is modelled by the following profile:

$$\begin{aligned} 2r_0(\psi) &= R_b + h_{\rm env} = R_* && 0.0 \le \psi < \psi_{\rm ap} \\ &= R_* + h_p\left(\frac{\psi}{\psi_a(\theta_t)} - \frac{\psi_{\rm ap}}{\psi_a(\theta_t)}\right)^2 && \psi_{\rm ap} \le \psi < \psi_{\rm bp} \\ &= R_b + \frac{r_c}{0.25}\left(0.25 - \left(\frac{\psi}{\psi_a(\theta_t)} - 0.5\right)^2\right) && \psi_{\rm bp} \le \psi < \psi_{\rm bt} \\ &= R_* + h_t\left(1.0 - \frac{\psi}{\psi_a(\theta_t)}\right)^2 && \psi_{\rm bt} \le \psi < \psi_a \\ &= R_b + h_{\rm env} = R_* && \psi_a \le \psi \le \psi^*. \end{aligned} \tag{24}$$

Here, R_* is the radius of the neutron star and is fixed at 10 km. R_b is the radius of the inner boundary. ψ^* and $\psi_a(\theta_t)$ are the same parameters used in the ring-shaped mound profile, and they vary with B_d and ζ, but now r_c is the maximum height of the mound above R_b. The new free parameters for this profile are as follows:

(i) $h_{\rm env}$ – This free parameter decides the depth of the current free neutron star envelope below R_*. The value of the inner radial boundary $R_b = R_* - h_{\rm env}$. Hence, the true height of the accreted mound above R_* will be given by $h_{\rm rel} = r_c - h_{\rm env}$.

(ii) $\psi_{\rm ap}$ – This parameter decides the extent of the ring-shaped mound near the pole, below this ψ is the envelope of the neutron star. This could be arbitrarily decided (since its value is dependent on the accretion profile) or it could be calculated from the light cylinder radius. When calculated from light cylinder constraints, for pulsars with periods in the range of 0.001–1 s, the angular extent of the open field lines on the neutron star surface from the pole varies from 27^0 to 0.8^0. We take a conservative estimate of 4^0 for the 10^{12} G pulsar assumed in this section.

The other new parameters that are dependent are calculated as follows:

(i) h_p and $\psi_{\rm bp}$ are calculated by ensuring continuity of $r_0(\psi)$ and $\frac{{\rm d}r_0}{{\rm d}\psi}$ at $\psi_{\rm bp}$.

(ii) h_t and $\psi_{\rm bt}$ are calculated by ensuring continuity of $r_0(\psi)$ and $\frac{{\rm d}r_0}{{\rm d}\psi}$ at $\psi_{\rm bt}$.

The $\psi_{\rm ap} \le \psi < \psi_{\rm bp}$ and $\psi_{\rm bt} \le \psi < \psi_a$ ranges define smooth transitions from the magnetostatic mound to the current free neutron star envelope. Since we need to have a particular value of initial B_d on the pole at R_*, we fix the value at R_b to $B_d \times (R_*/R_b)^3$. The gravitational acceleration term g is calculated using $g = \frac{GM_*}{R_b^2}$ (the mass of the neutron star is assumed to be unchanged as the envelope mass is relatively negligible). The calculation for θ_t was performed using the new inner boundary R_b. Fig. 11 describes the form of the new ring-shaped mound profile with an envelope for a specific set of parameters.

To demonstrate the effects of this profile on solutions, we choose a $B_d = 10^{12}$ G and an arbitrary $\theta_t = 50^0$ (similar to the solutions in the lower part of Fig. 6). Although the value of θ_t is not physically motivated, it helps to demonstrate the nature of the solutions with better θ resolution and larger mass, since θ resolution is higher near a higher θ_t. All solutions in this subsection have been calculated for a resolution of 5000 × 5000. The accreted mass is calculated after finding the total mass in the simulation domain and subtracting it

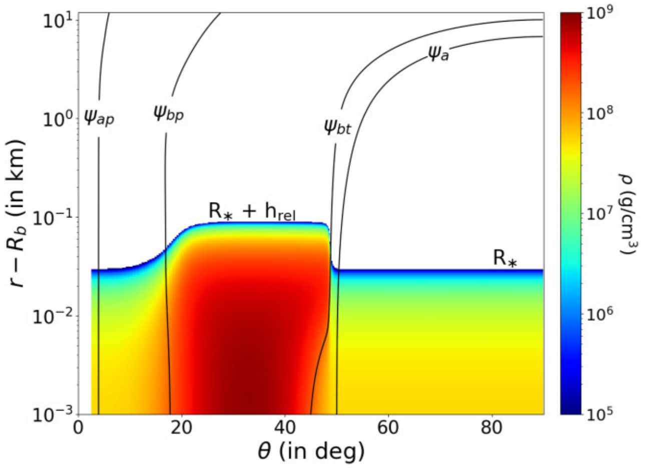

Figure 11. Density profile of the mound from equation (24) for parameters $B_d = 10^{12}$ G, arbitrary $\theta_t = 50^0$, arbitrary $\psi_{\rm ap} = \sin^2(4.0^0)$, $r_c = 90$ m, $h_{\rm env} = 30$ m, accreted mass $= 3.15 \times 10^{-9}$ M$_\odot$. Magnetic field lines for $\psi_{\rm ap}$, $\psi_{\rm bp}$, $\psi_{\rm bt}$ and ψ_a are also plotted here. The five regions separated by the field lines from $\theta = 0^0$ to $\theta = 90^0$ are the current free envelope, the transition region, the ring-shaped mound profile region, the transition region and the neutron star current free envelope, respectively.

Table 3. Radius of the neutron star is fixed at $R_* = 10$ km. For the same accreted mass 3.28×10^{-9} M$_\odot$, the values of $h_{\rm env}$ (depth below R_*), R_b (radius of inner boundary), r_c (mound height above R_b), absolute ellipticity, and dipole moment at the outer radius relative to the inner boundary is tabulated here.

$h_{\rm env}$ (m)	r_c (m)	R_b (km)	$\vert\epsilon\vert \times 10^{-9}$	$\tilde{\mu_1}(R_{\rm out})/\tilde{\mu_1}(R_b)$
0	90.1	10	2.885	0.9739
20	90.09	9.98	2.872	0.9737
30	90.43	9.97	2.86	0.9733
40	91.19	9.96	2.842	0.9723
50	92.58	9.95	2.818	0.9707
60	94.78	9.94	2.785	0.968
70	97.95	9.93	2.745	0.965

from the pre-existing envelope mass. This likely underestimates the accreted mass, since in a realistic scenario some of the pre-existing mass will be gravitationally compressed within the neutron star while the remaining mass will be mixed with the incoming accreted mass. We do not model such gravitational compression here.

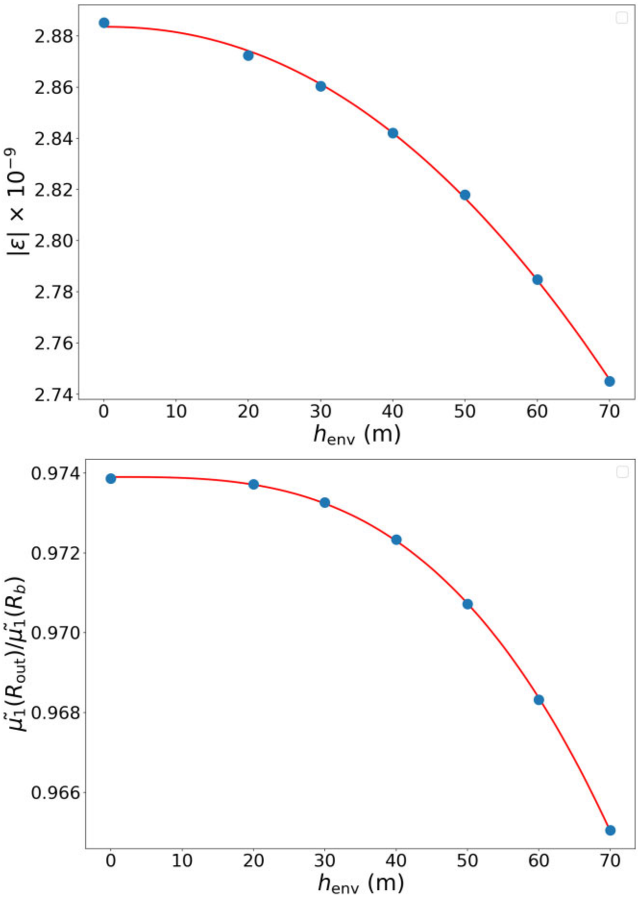

Figure 12. Absolute ellipticity versus envelope height (top plot) and normalized dipole moment at the outer radius with respect to the surface versus envelope height (bottom plot). Absolute ellipticity reduces and relative dipole moment decreases with increase in the envelope depth below the surface. Blue points in the plots is fitted to the function $y = ax^b + k$ with a red line. Fitting parameters are given in equations (25) and (24).

4.3.1 *Approximating sinking*

To understand the effect of sinking the same amount of accreted mass to different depths in the neutron star, we change the values of $h_{\rm env}$ or $h_{\rm rel} = r_c - h_{\rm env}$ (maximum height of the mound above the surface R_*). We compute GS solutions for seven different values of $h_{\rm env}$ (seven different R_b) such that the amount of accreted mass 3.28×10^{-9} M$_\odot$ is the same for all runs. The first solution with the same mass and $h_{\rm env} = 0.0$ is the pure ring-shaped mound profile without the pre-existing ocean, since for the ring-shaped mound profile $R_b = R_*$. The result for these simulations is noted in Table 3 and plotted in Fig. 12. Since $h_{\rm env}$ is the envelope depth below the surface R_*, an increase in $h_{\rm env}$ would imply a successive increase in the sinking of the mound. When the mound sinks, ellipticity and dipole moments both are seen to reduce in Fig. 12. Dipole moments are calculated with respect to the bottom radial boundary R_b, which is different for the seven examples. Considering gravitational compression will further reduce the ellipticity and will increase the value of dipole moments. Both absolute ellipticity and relative dipole moments are fitted with respect to the envelope depth as a red line in Fig. 12. The normalized dipole moment ratios are found to have the behaviour

$$\frac{\tilde{\mu_1}(R_{\rm out})}{\tilde{\mu_1}(R_b)} = 0.9739 - (2.02 \times 10^{-8} \times h_{\rm env}^{3.058}), \tag{24}$$

where $h_{\rm env}$ is in m, while absolute ellipticity is found to have the behaviour

$$\frac{|\epsilon|}{10^{-9}} = 2.8835 - (1.5 \times 10^{-5} \times h_{\rm env}^{2.145}), \tag{25}$$

where $h_{\rm env}$ is in m.

Wette et al. (2010) performed ideal MHD axisymmetric simulations on a neutron star by growing an accreted mound with an isothermal EOS either on a hard surface or inside a fluid base. For the same accreted mass and the same $\mathrm{d}M/\mathrm{d}\psi$, they found that the accretion mound grown inside a fluid base reduces the ellipticity by 25–60 per cent relative to the accretion mound grown on a hard surface. They calculated $h_{\rm env}$ by assuming the mass of the isothermal fluid base to be at least ten times the accreted mass. For the Paczynski EOS and the ring-shaped mound on ocean $r_0(\psi)$ (not same $\mathrm{d}M/\mathrm{d}\psi$), if a similar assumption of envelope mass equals ten times accreted mass ($M_{\rm env} = 10M_{\rm acc} = 3.28 \times 10^{-8}$ M$_\odot$) is made in this work, it is found that $h_{\rm env} = 112.6$ m and the absolute mass ellipticity is reduced by 13 per cent for the solution with this $h_{\rm env}$ and accreted mass relative to the pure ring-shaped mound profile.

4.3.2 *Fixing R_b*

In a realistic system, it is better to fix the depth at which magnetic fields are frozen from the crystallization properties of the crust. For an OCP (one component plasma), ion lattice melts at a Coulomb coupling parameter (i.e. electrostatic to thermal energy) $\Gamma_m \leq 175$ (Potekhin & Chabrier 2000). The density at which crystallization occurs depends on the temperature and composition of the crust. For an isolated cold neutron star, temperatures are low and matter is composed of iron (depending on the initial formation scenario and accretion process during the proto-neutron star stage) and thus ions crystallize at low densities such as 10^6 g cm^{-3} (Nättilä et al. 2024). However, an increase in temperature during accretion leads to higher crystallization densities. Also, accreted hydrogen helium matter undergoes burning at densities close to 10^5 g cm^{-3} (Brown & Bildsten 1998), adding hydrogen, helium, carbon and certain heavy elements till $Z = 26$ to the neutron star matter with certain mass fractions at different column depths which are dependent on the mass accretion rates (Brown & Bildsten 1998). This also changes the density at which matter is crystallized. For an accreting neutron star, we assume that crystallization occurs at a density of 10^9 g cm^{-3} (Brown & Bildsten 1998) and thus fix the magnetic fields at this density. From our chosen EOS and gravity, we can find the density at any prescribed depth assuming a constant height envelope. Thus, we decide to simulate for inner boundary density of 10^9 g cm^{-3}.

To understand the change in the solution with composition, we compare a solution with a composition of pure ionized helium matter ($\mu_e = 2.0$) and a composition of pure ionized iron ($\mu_e = 2.148$). For a neutron star with radius $R_* = 10$ km, the helium mound has a density of 10^9 g cm^{-3} at the inner radial boundary $R_b = 9.9074$ km, while an iron mound has a density of 10^9 g cm^{-3} at the inner radial boundary $R_b = 9.9158$ km i.e. at a lower depth. Now, we calculate the solutions for the two mounds with a different composition but with the same accreted mass of 1.85×10^{-8} M$_\odot$. We find the absolute ellipticity for the iron mound to be 7.75×10^{-9} which is higher than that of the helium mound: 6.67×10^{-9}. Dipole moments are also higher for the iron mound (0.746) relative to the helium mound (0.7).

Assuming a helium mound and fixing R_b at a density of 10^9 g cm^{-3} for an accreted mass 1.85×10^{-8} M$_\odot$, we find a latitudinally spreading mound profile with a pre-existing envelope as plotted in the bottom plot of Fig. 13. A ring-shaped mound profile with the same accreted mass has been plotted in the top plot of Fig. 13 for comparison. We have already deduced in the previous Section 4.3.1 that the sinking of the mound from the ring-shaped mound profile to the ring-shaped mound profile inside the neutron star envelope reduces the absolute ellipticities and the dipole moments. We can also observe from Fig. 13 that for the pure ring-shaped mound profile, the mound matter beyond θ_t is supported against gravity by a vacuum region and strong magnetic fields, while for the ring-shaped mound profile with the envelope, the mound matter beyond θ_t is supported against gravity by relatively low density matter and strong magnetic fields. Both the solutions are prone to MHD instabilities (Newcomb 1961; Goedbloed & Poedts 2004). But, a line-tying boundary condition provides stability to the system (Payne & Melatos 2007; Vigelius & Melatos 2008). However, it is difficult to determine the combined effects on the solutions without a non-linear evolution. Thus, the dynamical stability should be verified for both the mounds in a future work.

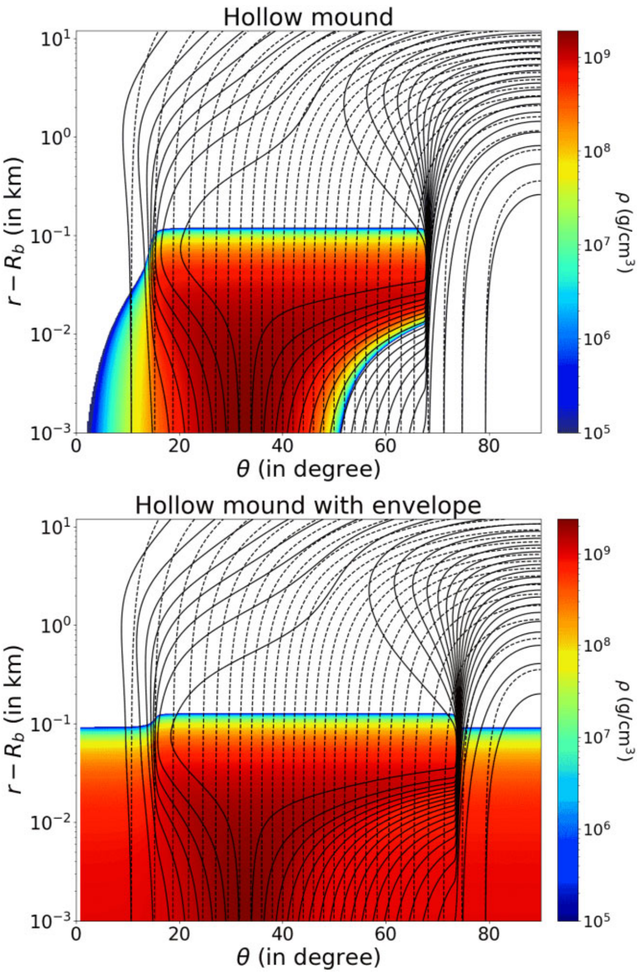

Figure 13. Density profiles and magnetic field lines (solid) for ring-shaped mound profile with ionized helium composition without envelope (top) and with envelope (middle). Dashed lines are the undistorted dipolar magnetic field lines. Density profile for the ring-shaped mound profile with ionized iron composition and with envelope is plotted at the bottom. Both the solutions have the same R_*, but a different domain inner boundary R_b. They also have the same amount of accreted mass.

5 QUADRUDIPOLAR INNER BOUNDARY FOR RING-SHAPED MOUND PROFILE

Multipolar magnetic fields were invoked to explain significant pair multiplication above the polar cap (Ruderman & Sutherland 1975). Recently, there has been strong observational evidence of relatively smaller X-ray thermal emission areas than expected, which have been explained due to the presence of multipolar magnetic fields (Geppert 2017; Rigoselli & Mereghetti 2018). However, Arumugasamy & Mitra (2019) has found that this estimation of the polarcap areas could be unreliable. Analysis of observations from NICER also suggests the presence of multipolar magnetic fields (Bilous et al. 2019; Chen et al. 2020; Kalapotharakos et al. 2021; Riley et al. 2021). Thus, neutron stars may have an intrinsic multipolar magnetic field before accretion from the binary companion begins. To understand the qualitative difference in the solutions relative to an initial dipolar field, we computed the GS solutions for an initial quadrudipolar field.

5.1 Description of the method

As noted in Fujisawa et al. (2022), quadrudipolar solution outside neutron star with radius R_* is

$$\psi(r,\theta) = \frac{\psi^* \sin^2\theta R_*}{r} + f_{\rm qd}\frac{\psi^* R_*^2 \sin^2\theta\cos\theta}{r^2}. \qquad (26)$$

Here, $\psi^* = \frac{1}{2}B_d R_*^2$ and $f_{\rm qd} = \frac{B_q}{B_d}$ (surface quadrupolar to dipolar strength fraction). The first term corresponds to a dipole and the second term is the quadrupolar term. For a neutron star with some quadrupolar contribution to the magnetic field, the angular extent of the simulations is from $\theta = 0^0$ (north magnetic pole) to $\theta = 180^0$(south magnetic pole) as the magnetic fields are not equatorially symmetric. At both $\theta = 0^0$ and $\theta = 180^0$, we assume $\psi = 0$. At $r = R_{\rm in}$, a fixed quadrudipolar field (equation 26) is assumed. For some quadrupolar contribution to the neutron star magnetic field, CFB condition equation for the outer radial boundary changes to (as both odd and even components contribute)

$$\psi(R_{\rm out},\theta') = \sum_{\ell=1}^{\ell_{\rm max}} \left(\frac{(2\ell+1)P_\ell^1(\cos\theta')sin\theta'}{2\ell(\ell+1)} \left(\frac{R_{\rm in}}{R_{\rm out}}\right)^{\ell} \times \int_{-1}^{1} \frac{\psi(R_{\rm in},\cos\theta)P_\ell^1(\cos\theta)}{\sqrt{1-\cos^2\theta}} d(\cos\theta) \right). \qquad (27)$$

The axisymmetric nature of the GS equation only allows us to model the dipolar and quadrupolar components of the field aligned to the magnetic axis with the accretion disc approaching the neutron star at the equator. We assume that the quadrupolar component is aligned parallel to the dipolar component.

The truncation angle (θ_t) calculation for a dipolar field is invalid for a quadrudipolar field as the Alfvén radius differs due to an extra radial field (from the quadrupolar component) at the equator. Çıkıntoğlu (2023) has made an estimation of the value of the Alfvén radius (R_{A^*}) for a non-rotating aligned quadrudipolar neutron star (axisymmetric assumption) by using conservation of angular momentum in steady state. For a particular B_q, B_d, $\dot{M}$ and certain accretion disc parameters α, ε, h/r, Alfvén radius (R_{A^*}) can be calculated from equation (24) in Çıkıntoğlu (2023) as

$$\left(\frac{R_{A^*}}{R_A}\right)^{3.5} + \beta\left(\frac{R_{A^*}}{R_A}\right)^{-2} = 1 \qquad (28)$$

where

$$\beta = \frac{27}{\alpha\sqrt{2}\varepsilon^{3.5}}\frac{h}{r}\left(f_{\rm qd}\right)^2 \frac{R_*^2}{R_A^2}.$$

Here R_A is the Alfvén radius for dipolar solution (equation 18). We have assumed $\dot{M}$ here to have the same value as the earlier dipolar simulations above, and $\alpha = 0.1$, $h/r = 0.1$, $\varepsilon = 1.0$ as assumed by Çıkıntoğlu (2023).

θ_t can be found from the roots of equation below, which is obtained by equating ψ at $\theta = 90^0$, $r = R_{A^*}$ (truncated accretion disc) to the ψ at $\theta = \theta_t$, $r = R_*$ (neutron star surface) as follows:

$$-f_{\rm qd}\cos^3\theta_t - \cos^2\theta_t + f_{\rm qd}\cos\theta_t + 1.0 - \frac{R_*}{R_{A^*}} = 0.0. \qquad (29)$$

The two roots of the equation above provide the values of θ_t in both the hemispheres.

5.2 Results

For any particular value of B_d and $f_{\rm qd}$, we calculate the Alfvén radius (R_{A^*}) from equation (28) and then subsequently θ_t. Beyond a certain $f_{\rm qd}$ (for a particular B_d and $\dot{M}$), no real solutions for R_{A^*} are found, as the strong quadrupolar field results in matter falling directly on the neutron star surface through the quadrupolar funnel (i.e. close to the blue dash–dotted line in the rightmost plot of Fig. 14). Fig. 14 shows the magnetic field lines in polar coordinates for three values of $f_{\rm qd}$. In this work, we choose the orientation of the quadrupolar field such that it lies in the direction of the dipolar field near the Magnetic North Pole (MNP; $\theta = 0^0$), while it is in the opposite direction to the dipolar field near the Magnetic South Pole (MSP; $\theta = 180^0$). Thus, the magnetic field is strengthened near the MNP while it gets weakened near the MSP making the field geometry asymmetric about the equator. As $f_{\rm qd}$ increases, the field geometry becomes more asymmetric and eventually the quadrupolar field dominates (as shown in Fig. 14). In the rightmost plot of Fig. 14 with $f_{\rm qd} = 5$, the black lines are the magnetic field lines with positive ψ i.e. in the direction of the dipolar magnetic field while the red lines are the magnetic field lines with negative ψ i.e. opposite direction to the dipolar magnetic field and in the direction of the quadrupolar field. Since for this case, the accretion disc at the equator is only threaded by the black field lines and not the red lines, matter is accreted near one of the poles and the equator. But after a certain higher $f_{\rm qd}$, the accreted matter will be channelled towards the neutron star surface through the quadrupolar funnel, following the radial field lines connecting to the equatorial region (see the blue dotted line in the rightmost plot of Fig. 14). We have used the ring-shaped mound profile for all cases here. We investigated for two values of B_d, as discussed below.

5.2.1 $B_d = 10^{10}$ G

GS solutions discussed in this section are for grids of size 10000 × 5000. Solutions can only be calculated using this method until $f_{\rm qd}$ of 1.0 since for $B_d = 10^{10}$ G and $f_{\rm qd} > 1.0$, matter channels directly through the quadrupolar funnel as discussed in the first paragraph of Section 5.2. The parameters and results for the different GS solutions have been noted in Table 4. The solutions have been evolved till the NMM for the current choice of grid size.

For a non-zero $f_{\rm qd}$, the angular extent of matter for the mound near the MSP is relatively higher than the angular extent of matter for the mound near MNP (Fig. 15). Some of the conclusions from the four cases (Table 4) are as follows:

(i) Case A ($f_{\rm qd} = 0.0$) – Two mounds at the two poles are symmetric and have the same mass, height, and angular extent.

(ii) Case B ($f_{\rm qd} = 0.1$) – As a small quadrupolar field is introduced, there is a lower mass mound near the MNP than the MSP, for the same maximum mound heights (r_c) at both the poles. Introduction of a quadrupolar field also increases the absolute mass ellipticity and the final heights of the mounds relative to the previous case.

(iii) Case C ($f_{\rm qd} = 1.0$, r_c(MNP) $= r_c$(MSP)) – As the surface quadrupolar field is further strengthened, mass near the MNP does not change significantly, but mass near the MSP increases by one order of magnitude relative to case B. Height of the two mounds near MNP and MSP is considered to be the same here (evolved till NMM for only the mound near MSP) as well but it is higher than the mounds in case B. Mass ellipticity for case C is 2.5 times higher relative to case B.

(iv) Case D ($f_{\rm qd} = 1.0$, r_c(MNP)$>r_c$(MSP)) – The heights of the mounds could differ near the two poles due to variations in the local mass accretion rates. Assuming a different height for case D, we evolve the solutions till NMM for the mounds near both MNP and MSP. The mass and height of the mound near MNP increase, while

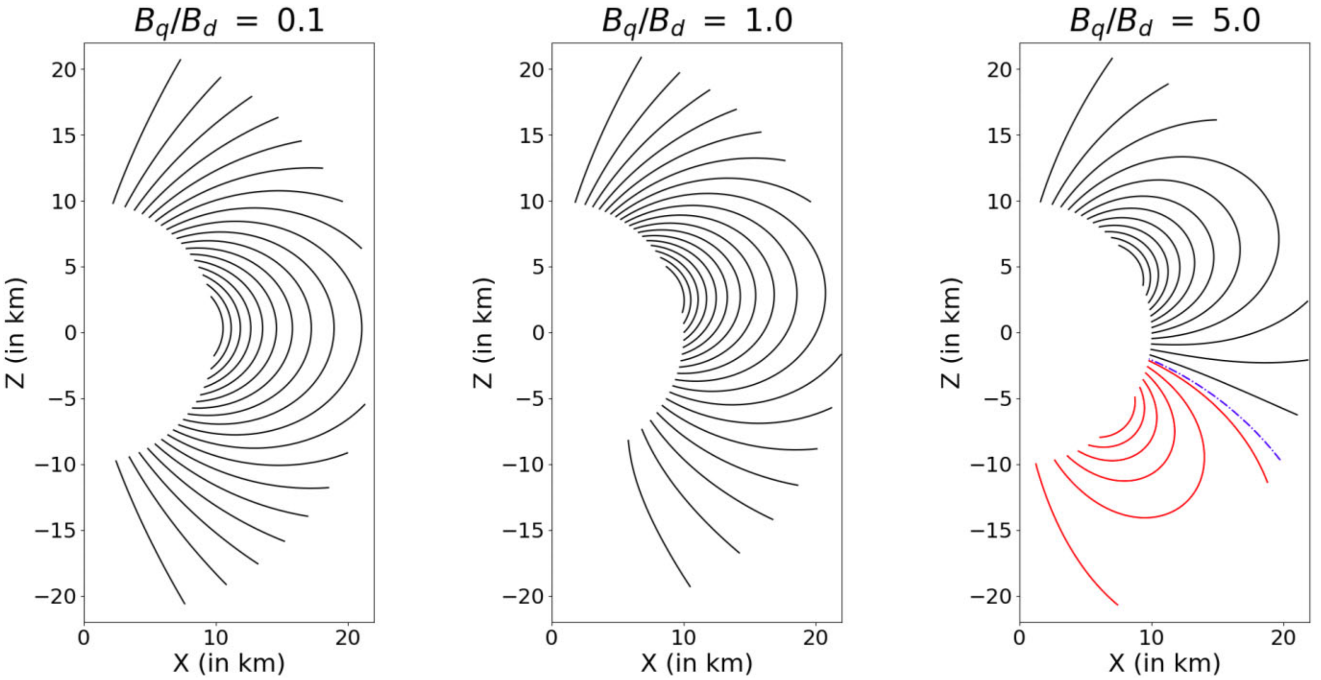

Figure 14. Polar plot of magnetic field lines for three different surface quadrupolar field to surface dipolar field ratios. Black lines are the magnetic field lines with positive ψ, while the red magnetic field lines are opposite to the black lines with negative ψ. Blue dotted line is the magnetic field line with $\psi = 0$. As $f_{\rm qd}$ increases from left to right, the equatorial asymmetry of the magnetic field geometry increases, while in the rightmost plot the quadrupole component dominates near the surface and thus the radial field is strong near the equator considerably helping the funnelling of matter.

Table 4. Accretion mound results for quadrudipolar inner boundary are tabulated here for two magnetic fields. $f_{\rm qd}$ is the surface quadrupole to dipole fraction. The truncation angle of the mound (θ_t), mass of the mound and maximum height of the mound (r_c) are noted down here for the two mounds near MNP and MSP. $|\epsilon|$ is the absolute ellipticity due to both the mounds.

Sr. No.	B_d (G)	$f_{\rm qd}$	$\lvert\epsilon\rvert$ (10^{-12})	MNP			MSP		
				θ_t	M (10^{-13} M$_\odot$)	r_c (m)	θ_t	M (10^{-13} M$_\odot$)	r_c (m)
A	10^{10}	0.0	1.47	21.7^0	4.659	11.33	158.3^0	4.659	11.33
B	10^{10}	0.1	1.55	20.7^0	4.337	11.45	157.17^0	5.53	11.45
C	10^{10}	1.0	3.91	17.575^0	4.39	13.14	132.36^0	42.09	13.14
D	10^{10}	1.0	3.96	17.575^0	4.73	13.38	132.36^0	42.09	13.14
E	10^{12}	1.0	2.3	4.0^0	0.55	20	158.22^0	14.9	20
F	10^{12}	5.0	8.6×10^{-4}	2.336^0	2.5×10^{-2}	10	101.42^0	6.4×10^{-2}	10

the mass and height of the mound near MSP are unchanged relative to the previous case.

Plots have been made for cases B and D on the left and right, respectively in Fig. 15. The ratios of normalized dipole moments for cases A, B, C, and D are 0.9989, 0.9986, 0.9954, and 0.9953, respectively. Changes in the dipole moment ratios are insignificant for these solutions. From these results, we can conclude that increasing the quadrupolar field (to a certain $f_{\rm qd}$) considerably increases the allowed mass of the mounds and also the mass ellipticity. In addition, it is possible to have a different height of the mound near both poles. Considering this may also add to the mass of the mounds and the ellipticity as a result of it.

5.2.2 $B_d = 10^{12}$ *G*

All results described in this section are for simulations with grids: 50000 × 2000 for an $R_{\rm out} - R_* = 2$ km. Solutions have been calculated using the method described in the previous Section 5.1 up to a $f_{\rm qd}$ of 5.0 since for $B_d = 10^{12}$ G and $f_{\rm qd} > 5.0$, matter channels directly through the quadrupolar funnel as discussed in the first paragraph of Section 5.2. Masses have not been calculated here upto NMM, since no significant change is expected in the qualitative output and such small angular extents require high angular resolution and thus high computational costs. The results of two cases E and F for representation have been presented here in Table 4 and Fig. 16 (top and bottom, respectively). Following are the inferences from the two cases :

(i) Case E ($f_{\rm qd} = 1.0$) – The angular extent of the mounds near both the poles are different, similar to case C, but since the magnetic field is higher here, the angular extent of the mounds is lower for this case relative to case C.

(ii) Case F ($f_{\rm qd} = 5.0$) – The mounds have a very low angular extent here due to the large surface magnetic field relative to the previous case E. The mounds are present near MNP and near the equator (close to 100^0) as the surface quadrupolar component dominates over the surface dipolar component. The mound near the equator has an extremely narrow angular extent (Fig. 16), but it has a mass greater than the mound near the pole.

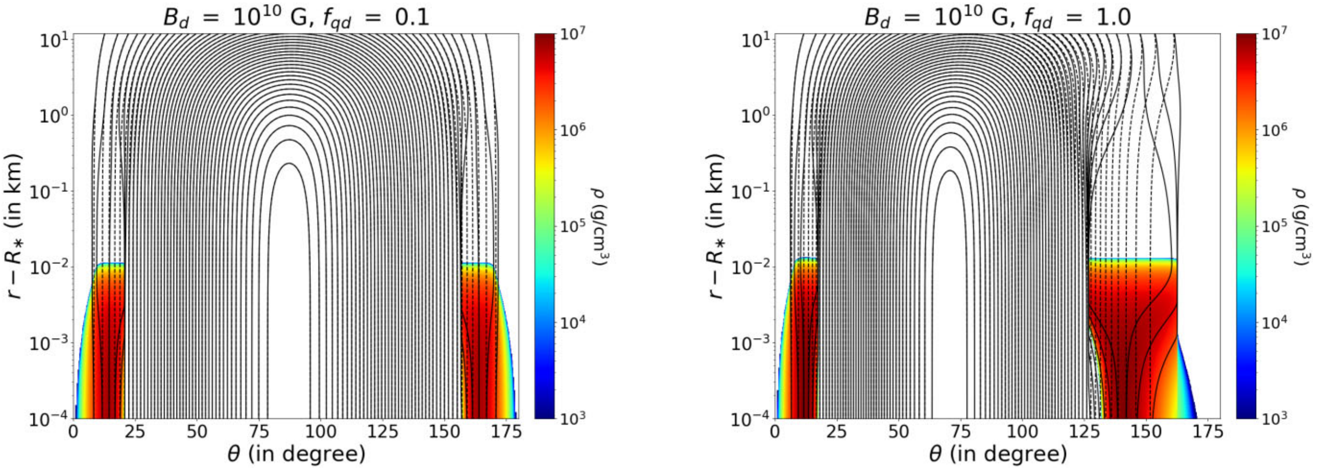

Figure 15. Plot of density profile and magnetic field lines (solid) for parameters $B_d = 10^{10}$ G and an initial quadrudipolar magnetic field of the neutron star. Plots have been made for case B (left) and case D (right). The quadrupole to dipole fractions (f_{qd}) have been indicated in the plots. Dashed lines are the initial undistorted quadrudipolar magnetic field lines. Increase in asymmetry due to a larger quadrupolar fraction can lead to a larger angular extent of the mass near one of the magnetic poles relative to the other pole (right plot).

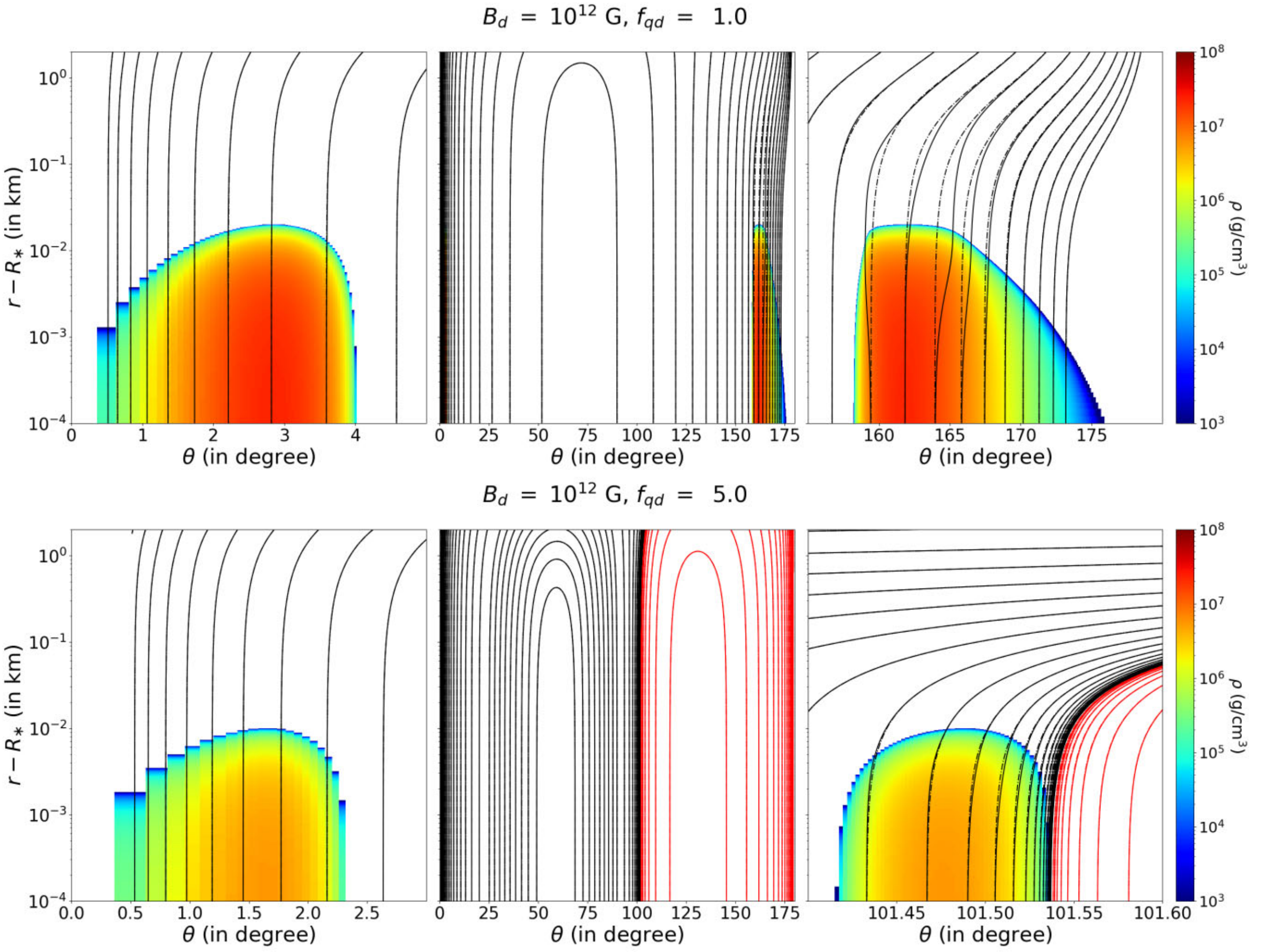

Figure 16. Plot of density profile and magnetic field lines (solid) for parameters $B_d = 10^{12}$ G and an initial quadrudipolar magnetic field of the neutron star. Plots have been made for case E (top middle) and case F (bottom middle). Red lines are magnetic field lines with negative ψ (opposite magnetic field direction (in the sense of clockwise or anticlockwise) to the black lines). The plots at the left and right of the middle plots are magnified plots of the mounds. Beyond a quadrupolar fraction, the angular extent of the mounds near MNP and equator becomes very narrow (bottom plot).

6 SUMMARY AND DISCUSSION

In this work, we have solved for the magnetic field geometry of accreted matter on a neutron star with a zero temperature degenerate electron gas EOS (Paczynski EOS) by the non-linear partial differential GS equation with zero toroidal field using the numerical relaxation method red black SOR. The numerical method is solved using an MPI framework and a new stretched radial coordinate that allows us to present solutions with improved resolution and an extended numerical domain. We have incorporated a new CFB condition at the outer radial boundary. Solutions for three profile functions ($r_0(\psi)$) have been discussed in this work. One of the profiles is a mound filled from the pole to the equator, with the profile decaying exponentially towards the equator. The ring-shaped mound profile first introduced in Mukherjee (2017) has been considerably used in this work. This profile accretes matter till an angle on the neutron star surface from the pole called the truncation angle θ_t. A physically motivated θ_t is the angle at which the magnetic field line from the NS surface connects the truncation radius r_t or the inner radius of the accretion disc. r_t is calculated here to be ζ times the Alfvén radius R_A.

We have explored a wide range of parameter space for the ring-shaped mound profile solutions by varying the maximum height r_c, magnetic field B_d ($10^9 - 10^{12}$ G), and multiple values of ζ ($\zeta = 0.6 - 1$ motivated from dynamic simulations e.g. Parfrey & Tchekhovskoy 2017; Parfrey et al. 2017). A physically motivated θ_t is used for a single accretion event. However, either cumulative accretion episodes or diffusion of matter over time could lead to matter accumulation till an arbitrarily large θ_t. Thus, in certain sections, we have used an arbitrary θ_t motivated by these possibilities. The pure ring-shaped mound profile assumes no pre-existing neutron star atmosphere and ocean. The third profile in this work is called the ring-shaped mound on ocean profile assuming accreted matter mixed into the pre-existing ocean and assuming no gravitational compression. We have attempted to calculate solutions by incorporating the effect of sinking using this profile. For all the profiles, we have calculated the accreted mass, absolute ellipticity and dipole moment at the outer radius relative to the NS surface. The solutions for the above three profiles have been calculated by using a dipolar magnetic field at the inner boundary. We have also calculated solutions for a quadrudipolar magnetic field at the inner boundary by using only the ring-shaped mound profile and by varying the surface quadrupole to dipole fractions.

Some of the important inferences from this work are as follows:

(i) **Current free boundary**: The CFB condition is found to be more efficient than other boundary conditions. We have demonstrated in Figs 3 and 4 that the solution using the CFB is independent of the chosen domain size unlike the fixed and free boundary.

(ii) **Spreading ring-shaped mound profile solutions**: The ring-shaped mound profile is found to latitudinally spread with an increase in mass. The ring-shaped mound profile does not show closed magnetic loops in the solution beyond a certain mass like the filled mound profiles because magnetic field lines are stretched in both directions, i.e. direction of the equator and direction of the poles. The ring-shaped mound profile is more physically motivated than the filled mound since the ring-shaped mound profile populates relatively lower mass on open magnetic field lines near the magnetic pole. Such spreading solutions have significant implications as outlined in the next point.

(iii) **Implications for field burial**: From the spreading solutions, we have demonstrated the onset of field burial. The efficiency of field burial depends on the extent of the angular spread of the accreted matter, beyond the confinement from θ_t at the base. For the assumed ring-shaped mound profile and a physically motivated θ_t, we find the solutions to be non-unique beyond a particular mass we call the NMM (Appendix C) and this NMM is limited by resolution. We have evolved all solutions till NMM by considering a single resolution, to evaluate qualitative trends of various physical quantities. Lowest dipole moment values (or maximum field burial) calculated for the four B_d values are noted in Table 5. We show field burial to be effective for the low field pulsars. This is evident for the solution with $B_d = 10^9$ G and $\zeta = 0.6$ which has a dipole moment reduction of 37 per cent and has a mound latitudinally spread till the equator. We could not show significant field burial for the high magnetic field pulsars since these solutions have not been explored to a maximum field burial possible i.e they have not been evolved till they latitudinally spread to the equator. Such an endeavour will require larger resolution and grid sizes, to go beyond the current limitations posed by the maximum numerical mass. This will be explored in a future work.

Table 5. For the four magnetic fields and for the ring-shaped mound profile, NMM, time taken to accrete the mound masses ($T_{\rm acc}$), the relative dipole moment $\tilde{\mu_1}(R_{\rm out})/\tilde{\mu_1}(R_*)$ has been noted down in the table for the case $\zeta = 0.6$ (i.e. the case with the maximum masses and lowest dipole moments).

B_d (G)	NMM (10^{-12} M$_\odot$)	$T_{\rm acc}$ (hours)	$\tilde{\mu_1}(R_{\rm out})/\tilde{\mu_1}(R_*)$
10^9	20.18	9.11	0.627
10^{10}	41.92	18.93	0.894
10^{11}	134.91	60.92	0.991
10^{12}	214.2	96.72	0.999

Table 5 has noted down the maximum mass found by our solutions for the four magnetic fields and the time taken to accrete these masses. We can observe that we have modelled mounds tha have been accreted on to the surface of the neutron star in a few hours to few days, i.e. the very initial accretion phase of a single outburst event. Patruno (2012) interpreted the exponential decay of spin frequency derivative from the X-ray data of a pulsar as evidence of magnetic field burial. The timescales required to accrete the masses and the magnetic screening found by our ring-shaped mound solutions provide support to this argument of short term field burial. Accretion mound solutions can also be calculated for an arbitrary choice of θ_t which may be the result of cumulative accretion episodes. For example, in Section 4.2.1, we find the lowest dipole moment to be 0.43 for a solution with $B_d = 10^{12}$ G and an arbitrary $\theta_t = 50^0$ for a mound latitudinally spread till the equator.

(iv) **Ring-shaped mound on ocean**: For the ring-shaped mound profile, matter at an angle greater than θ_t is supported by vacuum and strong magnetic fields, but for the ring-shaped mound with the envelope, matter at an angle greater than θ_t is supported by a relatively less dense envelope and strong magnetic fields, thus increasing the chance of stability. By approximating sinking using this profile, we find that sinking of the same amount of accreted mass ignoring gravitational compression reduces the absolute mass ellipticity and dipole moments. A change in composition from helium to iron does not cause a significant change in the final solutions. Using this profile, we suggest choosing the inner boundary inside the neutron star to fix the magnetic fields based on the current crystallization properties of the crust in any future work to model a realistic system. The results for the pure ring-shaped mound profile provide upper limits to the mass and absolute ellipticity of the ring-shaped mound on the ocean.

(v) **Quadrudipolar magnetic fields**: Due to a quadrupolar field in addition to the dipolar field, the magnetic field gets stronger near one pole and weaker near the other pole (middle plot of Fig. 14). As the quadrupole to dipole fraction further increases, the dipolar magnetic field is strengthened by the quadrupolar field near one pole while the quadrupolar field dominates near another pole (rightmost plot of Fig. 14). From the calculation of angular extents from Alfvén radius constraints for the quadrudipolar magnetic fields, it is found that the angular extent of the mound near one magnetic pole decreases relative to the other magnetic pole. Due to this, asymmetric mounds are accreted with a different mass and different heights near the two magnetic poles. Eventually, beyond a certain large $f_{\rm qd}$ limit (1.0 for $B_d = 10^{10}$ G and 5.0 for $B_d = 10^{12}$ G), mass should flow through the quadrupolar funnel (blue dotted line in the rightmost plot of Fig. 14) and these solutions cannot be modelled by the method used in this work. The mass flow through the quadrupolar funnel is depicted in GRMHD simulations of accreting neutron stars in Das, Porth & Watts (2022). Through preliminary analysis, we find that as the quadrupole field to dipole field fraction increases, the equatorial asymmetry of the magnetic field geometry, the mass and absolute ellipticity of the accretion mounds increase. Instead of using Alfvén radius constraints, Fujisawa et al. (2022) populates matter on all the magnetic field lines in both hemispheres. This is unlikely to happen from a single accretion episode, but it is possible for the case of fallback accretion on central compact objects (CCOs).

Limitations of this work are noted down below

(i) **Numerical maximum mass**: NMM is limited by resolution and thus limits the mass of the solutions presented here (Appendix C). In a future work, we will attempt to find the maximum mass of the solutions limited by physical restraints by modelling GS solutions on very large grid sizes to accommodate equator-ward spread from a polar cap based accretion profile. Such solutions will utilize the numerical framework established in this paper and the preliminary results presented here to compute large-scale solutions on extended grids.

(ii) **No fixed mass-loading per flux tube between different solutions**: Following Mukherjee & Bhattacharya (2012), Mukherjee (2017), and Fujisawa et al. (2022), we assume an analytical profile function ($r_0(\psi)$) without explicit constraints on the form of mass distribution per flux tube ($\mathrm{d}M/\mathrm{d}\psi$). Magnetostatic solutions are obtained by a numerical relaxation method for an initially unknown particular $dM/d\psi$. One of the limitations in using such an analytical profile function $r_0(\psi)$ is that two different GS solutions, such as with different maximum height (r_c), will have different mass loading profile per field line ($dM/d\psi$). But, it does not mean that the solutions found here are incorrect. Each solution gives a possible equilibrium configuration for a given mass, although with a different $dM/d\psi$. In future, if a long-term burial is to be modelled, the solution framework needs to be adapted to conserve the mass-loading at different iteration steps (e.g. Payne & Melatos 2004; Priymak et al. 2011).

(iii) **Artificial treatment of mixing and sinking**: Through axisymmetric MHD simulations, Wette et al. (2010) found that sinking reduces the ellipticity by 25–60 per cent for an isothermal EOS. For the Paczynski EOS, we find that sinking reduces ellipticity, but not as significantly as the above work. But, we ignore gravitational compression and we have not treated sinking and mixing of matter dynamically. This problem must be explored dynamically.

(iv) **No GR effects**: Rossetto et al. (2023) numerically solved the general relativistic formulation of the Grad Shafranov equation (GRGS) for an isothermal EOS. After comparing the dimensionless dipole moment, they found that the GRGS solutions show approximately three times less screening than the Newtonian GS solutions. In addition, the characteristic scale height of the mound is reduced by 40 per cent for GRGS solutions for an isothermal EOS. The current work explores the efficacy of the CFB for a Newtonian framework for ease of applicability. For any future work, GS formalism and the CFB condition should be extended to a GR framework for a better self-consistent treatment of the problem.

(v) **Stability of the mounds**: The stability of accretion mounds has been probed by various authors (Payne & Melatos 2007; Vigelius & Melatos 2008, 2009b) through MHD simulations, and they find axisymmetric stability and non-axisymmetric modes making the mounds unstable. Mukherjee et al. (2013a) performed axisymmetric 2D MHD simulations of a section of the mound and found that the mounds are stable to interchange instabilities when perturbed but increasing the mass of the mound destabilizes the mound. Mukherjee et al. (2013b) performed 3D MHD simulations of the same in PLUTO and found multiple radially elongated streams in the azimuthal direction due to pressure-driven toroidal instabilities. Kulsrud & Sunyaev (2020), through an analytical analysis, suggest that an efficient mechanism based on a strong ideal Schwarzschild instability will be responsible for mass flow across flux surfaces or magnetic field lines (instability creates a cascade of eddies down to resistive scales at which the mass flow occurs). Although the above results predict and demonstrate the onset of MHD instabilities, the nature of the solutions in the non-linear saturation regime is not well known. Vigelius & Melatos (2009a) through MHD analysis predict that a non-axisymmetric equilibria may be achieved starting from the unstable GS solutions. The stability of the mound profiles described in this work needs to be explored using dynamical simulations. Non-ideal effects such as resistivity (Vigelius & Melatos 2009b) and thermal conduction (Suvorov & Melatos 2019) should also be included in such simulations.

(vi) **Mass accretion rate**: The mass accretion rate has been assigned to an arbitrarily high value here, which is the same for all B_d. This may not be true, and the values of the mass accretion rate should be motivated in future simulations by observations.

(vii) **No toroidal field**: Fujisawa et al. (2022) found that a large toroidal field can be present inside the mounds, although this does not significantly affect the GS solutions. There will be an attempt in the future to check the effects of toroidal fields on our solutions.

ACKNOWLEDGEMENTS

The authors are thankful to the anonymous referee for the thorough review and detailed suggestions that helped improve the clarity and presentation of the article. We gratefully acknowledge the use of high performance computing facilities at IUCAA, Pune.[3] Dipanjan Mukherjee thanks Yuri Levin for a discussion on the idea of a current free boundary condition. The authors thank Ashwin Devaraj for his useful input on our plots. The authors also thank Prathamesh Ratnaparkhi for useful discussions on finding NMM.

DATA AVAILABILITY

No new data was generated in support of this research. The simulations used in this work are available from the corresponding authors upon reasonable request.

---

[3] http://hpc.iucaa.in

REFERENCES

Alford M. G., Schwenzer K., 2014, ApJ, 781, 26
Alpar M. A., Cheng A. F., Ruderman M. A., Shaham J., 1982, Nature, 300, 728
Arons J., Lea S. M., 1976a, ApJ, 207, 914
Arons J., Lea S. M., 1976b, ApJ, 210, 792
Arons J., Lea S. M., 1980, ApJ, 235, 1016
Arumugasamy P., Mitra D., 2019, MNRAS, 489, 4589
Baym G., Pethick C., Pines D., Ruderman M., 1969, Nature, 224, 872
Becker P. A., Wolff M. T., 2007, ApJ, 654, 435
Bessolaz N., Zanni C., Ferreira J., Keppens R., Bouvier J., 2008, A&A, 478, 155
Bildsten L., 1998, ApJ, 501, L89
Bilous A. V. et al., 2019, ApJ, 887, L23
Bisnovatyi-Kogan G. S., Komberg B. V., 1974, Soviet Ast., 18, 217
Blandford R. D., Decampli W. M., Konigl A., 1979, in Bulletin of the American Astronomical Society, 11, 703
Blondin J. M., Freese K., 1986, Nature, 323, 786
Bonazzola S., Gourgoulhon E., 1996, A&A, 312, 675
Brown E. F., Bildsten L., 1998, ApJ, 496, 915
Caiazzo I., Heyl J., 2021, MNRAS, 501, 109
Chandrasekhar S., 1970, Phys. Rev. Lett., 24, 611
Chatterjee D., Novak J., Oertel M., 2021, Eur. Phys. J. A, 57, 249
Chen A. Y., Yuan Y., Vasilopoulos G., 2020, ApJ, 893, L38
Choudhuri A. R., Konar S., 2002, MNRAS, 332, 933
Coburn W., Heindl W. A., Rothschild R. E., Gruber D. E., Kreykenbohm I., Wilms J., Kretschmar P., Staubert R., 2002, ApJ, 580, 394
Cumming A., Zweibel E., Bildsten L., 2001, ApJ, 557, 958
Cutler C., 2002, Phys. Rev. D, 66, 084025
Das P., Porth O., Watts A. L., 2022, MNRAS, 515, 3144
Fattoyev F. J., Horowitz C. J., Lu H., 2018, preprint (arXiv:1804.04952)
Friedman J. L., Schutz B. F., 1978, ApJ, 222, 281
Fujisawa K., Kisaka S., Kojima Y., 2022, MNRAS, 516, 5196
Geppert U., 2017, JA&A, 38, 46
Giliberti E., Cambiotti G., 2022, MNRAS, 511, 3365
Goedbloed J. P. H., Poedts S., 2004, Principles of Magnetohydrodynamics. Cambridge Univ. Press, Cambridge
Haensel P., Potekhin A. Y., Yakovlev D. G., 2007, Neutron Stars 1: Equation of State and Structure, Vol. 326. Springer, New York
Hameury J. M., Bonazzola S., Heyvaerts J., Lasota J. P., 1983, A&A, 128, 369
Haskell B., Antonelli M., Pizzochero P., 2022, Universe, 8, 619
Istomin Y. N., Semerikov I. A., 2016, MNRAS, 455, 1938
Jahan Miri M., Bhattacharya D., 1994, MNRAS, 269, 455
Jones D. I., 2010, MNRAS, 402, 2503
Kalapotharakos C., Wadiasingh Z., Harding A. K., Kazanas D., 2021, ApJ, 907, 63
Kerin A. D., Melatos A., 2022, MNRAS, 514, 1628
Konar S., 2017, JA&A, 38, 47
Konar S., Bhattacharya D., 1997, MNRAS, 284, 311
Konar S., Bhattacharya D., 1999a, MNRAS, 303, 588
Konar S., Bhattacharya D., 1999b, MNRAS, 308, 795
Konar S., Choudhuri A. R., 2004, MNRAS, 348, 661
Kulkarni A. K., Romanova M. M., 2013, MNRAS, 433, 3048
Kulsrud R. M., Sunyaev R., 2020, J. Plasma Phys., 86, 905860602
Lattimer J. M., Prakash M., 2004, Science, 304, 536
Lindblom L., Mendell G., 1995, ApJ, 444, 804
Long M., Romanova M. M., Lovelace R. V. E., 2005, ApJ, 634, 1214
Mastrano A., Suvorov A. G., Melatos A., 2015, MNRAS, 447, 3475
Melatos A., Payne D. J. B., 2005, ApJ, 623, 1044
Melatos A., Phinney E. S., 2001, PASA, 18, 421
Melatos A., Douglass J. A., Simula T. P., 2015, ApJ, 807, 132
Mukherjee D., 2017, JA&A, 38, 48
Mukherjee D., Bhattacharya D., 2012, MNRAS, 420, 720
Mukherjee D., Bhattacharya D., Mignone A., 2013a, MNRAS, 430, 1976
Mukherjee D., Bhattacharya D., Mignone A., 2013b, MNRAS, 435, 718
Mukherjee D., Bult P., van der Klis M., Bhattacharya D., 2015, MNRAS, 452, 3994
Muslimov A. G., Tsygan A. I., 1985, Soviet Astron. Lett., 11, 80
Mytidis A., Coughlin M., Whiting B., 2015, ApJ, 810, 27
Nättilä J., Cho J. Y. K., Skinner J. W., Most E. R., Ripperda B., 2024, ApJ, 971, 37
Nazari E., Roshan M., 2020, MNRAS, 498, 110
Newcomb W. A., 1961, Phys. Fluids, 4, 391
Owen B. J., 2010, Phys. Rev. D, 82, 104002
Paczynski B., 1983, ApJ, 267, 315
Pandharipande V. R., Pines D., Smith R. A., 1976, ApJ, 208, 550
Parfrey K., Tchekhovskoy A., 2017, ApJ, 851, L34
Parfrey K., Spitkovsky A., Beloborodov A. M., 2017, MNRAS, 469, 3656
Patruno A., 2012, ApJ, 753, L12
Payne D. J. B., Melatos A., 2004, MNRAS, 351, 569
Payne D. J. B., Melatos A., 2007, MNRAS, 376, 609
Potekhin A. Y., Chabrier G., 2000, Phys. Rev. E, 62, 8554
Press W. H., Teukolsky S. A., Vetterling W. T., Flannery B. P., 1992, Numerical Recipes in C. The Art of Scientific Computing. Cambridge Univ. Press, Cambridge
Priymak M., Melatos A., Payne D. J. B., 2011, MNRAS, 417, 2696
Priymak M., Melatos A., Lasky P. D., 2014, MNRAS, 445, 2710
Psaltis D., Chakrabarty D., 1999, ApJ, 521, 332
Radhakrishnan V., Srinivasan G., 1984, in Hidayat B., Feast M. W., eds, Second Asian-Pacific Regional Meeting on Astronomy. p. 423
Rigoselli M., Mereghetti S., 2018, A&A, 615, A73
Riles K., 2023, Living Rev. Relativ., 26, 3
Riley T. E. et al., 2021, ApJ, 918, L27
Romani R. W., 1990, Nature, 347, 741
Romanova M. M., Kulkarni A. K., Lovelace R. V. E., 2008, ApJ, 673, L171
Rossetto P. H. B., Frauendiener J., Brunet R., Melatos A., 2023, MNRAS, 526, 2058
Rossetto P. H. B., Frauendiener J., Melatos A., 2025, ApJ, 979, 10
Ruderman M., 1969, Nature, 223, 597
Ruderman M., 1991a, ApJ, 366, 261
Ruderman R., 1991b, ApJ, 382, 576
Ruderman M. A., Sutherland P. G., 1975, ApJ, 196, 51
Singh N., Haskell B., Mukherjee D., Bulik T., 2020, MNRAS, 493, 3866
Smarr L. L., Blandford R., 1976, ApJ, 207, 574
Srinivasan G., Bhattacharya D., Muslimov A. G., Tsygan A. J., 1990, Curr. Sci., 59, 31
Sur A., Haskell B., 2021a, PASA, 38, e043
Sur A., Haskell B., 2021b, MNRAS, 502, 4680
Suvorov A. G., Melatos A., 2019, MNRAS, 484, 1079
Suvorov A. G., Melatos A., 2020, MNRAS, 499, 3243
Taam R. E., van den Heuvel E. P. J., 1986, ApJ, 305, 235
Trottenberg U., Oosterlee C. W., Schuller A., 2000, Multigrid. Academic press
Urpin V., Geppert U., 1995, MNRAS, 275, 1117
Urpin V., Konenkov D., 1997, MNRAS, 284, 741
Vigelius M., Melatos A., 2008, MNRAS, 386, 1294
Vigelius M., Melatos A., 2009a, MNRAS, 395, 1972
Vigelius M., Melatos A., 2009b, MNRAS, 395, 1985
Wette K., Vigelius M., Melatos A., 2010, MNRAS, 402, 1099
Zanni C., Ferreira J., 2009, A&A, 508, 1117
Zimmermann M., 1978, Nature, 271, 524
Çıkıntoğlu S., 2023, MNRAS, 524, 3846

APPENDIX A: NUMERICAL METHOD

For the logarithmic coordinates (y, μ) used here, $\mathrm{d}r$ (spherical coordinates (r, θ)) is given by

$$\mathrm{d}r = (r - aR_*)\,\mathrm{d}y.$$

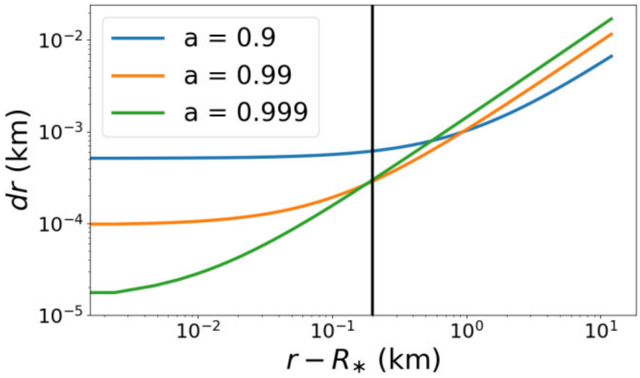

Figure A1. The value of dr is plotted as a function of $r - R_*$, both in km for three values of a and for the logarithmic radial coordinates used in this work. The vertical line is at 200 m above the neutron star surface i.e approximately the maximum heights of mounds used in this work.

The radial extent of the grid lies between R_* and $R_{\rm out}$ i.e. $y_1 = 0$ and $y_2 = \log((R_{\rm out} - aR_*)/(R_*(1-a)))$. Let N_y be the number of points between y_1 and y_2. Thus, $\mathrm{d}y = (y_2 - y_1)/(N_y + 1)$. Therefore,

$$\mathrm{d}r = \frac{(r - aR_*)}{(N_y + 1)} \log\left(\frac{R_{\rm out} - aR_*}{R_*(1-a)}\right). \tag{A1}$$

For fixed R_*, $R_{\rm out}$, and N_y, the value of dr depends on r and a. This dependence has been plotted in Fig. A1 for $R_* = 10$ km, $R_{\rm out} = 22$ km, $N_y = 5000$ and three values of a. From Fig. A1, we can see that as the value of a increases, the stretching of the radial grid increases. The vertical line in Fig. A1 has been plotted for a height 200 m above the surface. The heights less than 200 m are better resolved by $a = 0.999$ relative to the smaller values of a. Since the mounds in this work are close to 200 m or do not exceed 200 m, we selected an optimal value of $a = 0.999$ for all calculations. For $a = 0.999$ and for a resolution of 5000 points, the value of dr varies from 0.01419 m at the inner boundary to 17 m at the outer radial boundary. The typical scale heights of the solutions (e.g. 1–1000 m for the solution in Section 3.2.2) are resolved by the selected grid. Equation 11 can be written in second order finite differenced form as follows:

$$\begin{aligned} &y_c^{+}\psi[y + \Delta y;\mu] + y_c^{-}\psi[y - \Delta y;\mu] + e_c\psi[y;\mu] \\ &+\mu_c(\psi[y;\mu + \Delta\mu] + \psi[y;\mu - \Delta\mu]) \\ &= src_{\rm coeff}K(\psi[y;\mu], y, \mu), \end{aligned} \tag{A2}$$

where

$$\begin{aligned} y_c^{+} &= (\Delta\mu)^2 - \frac{(\Delta\mu)^2(\Delta y)}{2}, \\ y_c^{-} &= (\Delta\mu)^2 + \frac{(\Delta\mu)^2(\Delta y)}{2}, \\ \mu_c &= \frac{(1-\mu^2)(\Delta y)^2}{\left(1 + \frac{a}{e^{y}(1-a)}\right)^2}, \\ e_c &= \left(-2(\Delta\mu)^2 - 2(\Delta y)^2\frac{(1-\mu^2)}{\left(1 + \frac{a}{e^{y}(1-a)}\right)^2}\right), \\ src_{\rm coeff} &= (\Delta y)^2(\Delta\mu)^2R_*^2(1-a)^2e^{2y}, \end{aligned}$$

and $K(\psi, y, \mu)$ is the source function from equation (9).

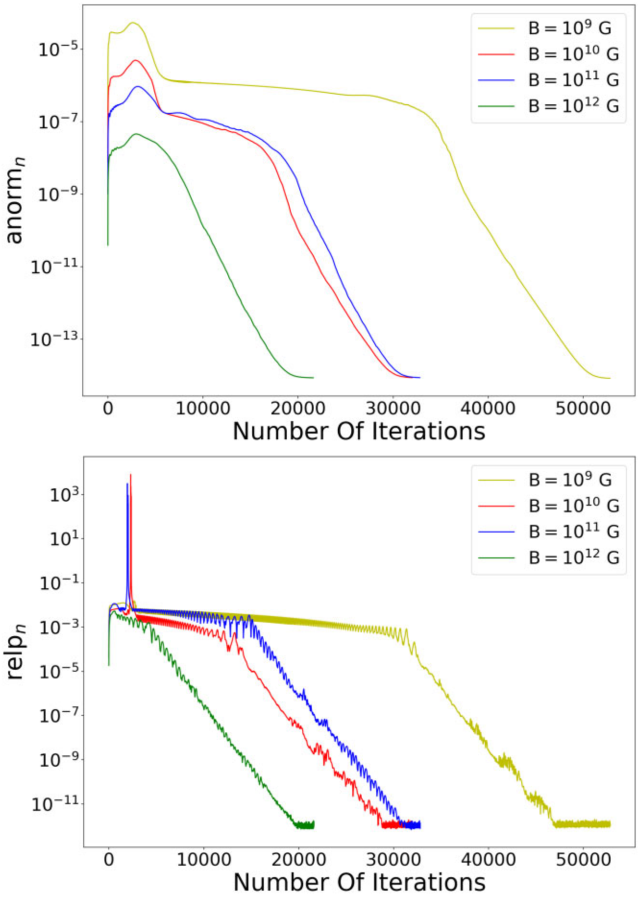

Figure A2. Change in the value of $anorm_n$ (top) and in the value of $relp_n$ (bottom) with the number of iteration steps for 4 magnetic field strength cases have been plotted. Simulations are stopped after both show evidence of flattening out. All cases have been plotted for Maximum Mass solutions.

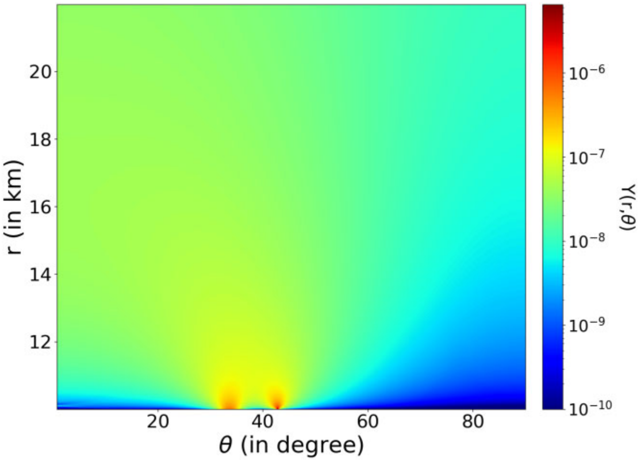

Figure A3. Absolute relative difference between the solution using our current local SOR-Picard method and the solution using the old global SOR-underrelaxation method.

A dipolar solution is used as an initial guess and red black SOR algorithm is used to iteratively update ψ to solve the equation (A2). The RHS or the source term of equation (A2) is updated at each step using the value of the solution at the previous SOR step. All boundary conditions are updated at each SOR step using the solution at the previous step. Earlier studies have often used a two-layer relaxation method with a first layer of SOR having the source constant for each SOR iteration, followed by an under-relaxation with an update of the RHS, and a repetition of these steps till convergence. However, in this study we have employed a local relaxation method called the SOR-Picard method (Trottenberg, Oosterlee & Schuller 2000) without under-relaxation, which is faster. In the new method, ψ is relaxed by SOR and the non-linear RHS term is updated at each SOR iteration using the ψ from the previous iteration. The iteration is stopped after the values of anorm$_n$ and relp$_n$ (n =Number of the iteration step) flatten out or remain unchanged. This criteria for convergence, although more restrictive, is more robust, than stopping at an arbitrary value. Their values are calculated by

$$\begin{aligned}\mathrm{anorm}_n =& \sum_{i,j} |y_c^+\psi[y_i+\Delta y;\mu_j] + y_c^-\psi[y_i-\Delta y;\mu_j]\\ &+(e_c)_{i,j}(\psi[y_i;\mu_j])\\ &+(\mu_c)_{i,j}(\psi[y_i;\mu_j+\Delta\mu]+\psi[y_i;\mu_j-\Delta\mu])\\ &-(src_{\mathrm{coeff}})_{i,j}K(\psi[y_i;\mu_j],y_i,\mu_j)| \qquad \text{(A3)}\\ \mathrm{relp}_n =& MAX\left(\frac{|\psi_{n+1}(y_i,\mu_j)-\psi_n(y_i,\mu_j)|}{\psi_{n+1}(y_i,\mu_j)}\right).\end{aligned}$$

An example of the change in anorm$_n$ and relp$_n$ with the number of iteration steps is shown in Fig. A2. The examples plotted here are for the NMM (refer to Appendix C) of the solutions, with high gradients at some points.

A1 Optimal ω for SOR

From Press et al. (1992), the optimal choice of ω (overrelaxation parameter) for SOR is

$$\omega = \frac{2}{1+\sqrt{1-\rho^2_{\mathrm{Jacobi}}}}, \qquad \text{(A4)}$$

where ρ_{Jacobi} is the spectral radius of the Jacobi iteration. ρ_{Jacobi} for the 2D Poisson equation on a rectangular $J \times L$ grid is (Press et al. 1992)

$$\rho_{\mathrm{Jacobi}} = \frac{\cos\frac{\pi}{J} + \left(\frac{\Delta x}{\Delta y}\right)^2 \cos\frac{\pi}{L}}{1+\left(\frac{\Delta x}{\Delta y}\right)^2}. \qquad \text{(A5)}$$

Calculating ρ_{Jacobi} for a general elliptic equation is non-trivial since the eigenvalues of the iteration matrix for such equations have spatial dependence. Empirical testing of different values of ω showed that the form of the spectral radius in equation (A5) is optimal and adequate for the GS equation (A2).

A2 Checking with global SOR-underrelaxation method

For global SOR-underrelaxation method (earlier method), Chebyshev acceleration is used for SOR while an underrelaxation parameter of 0.01 is used (Mukherjee & Bhattacharya 2012). Fig. A3 represents the colourmap of the absolute relative difference between the solution from global SOR-underrelaxation method and the solution from local relaxation SOR Picard method. The plot shows that the solutions match by up to 10^{-5}. Hence, the new method gives solutions that match well with those from the earlier method.

APPENDIX B: OUTER RADIAL CURRENT FREE BOUNDARY CONDITION

The derivation of the CFB condition is presented in the first Section B1. In the subsections following the first, a series of tests were performed on the new CFB condition (for the dipolar case) to optimize it and test its validity.

B1 Derivation

If L is the GS operator and L^* is the adjoint operator, then we need to solve the problem

$$L\psi = f,$$

where f is the source function. Using Green's theorem, and from equation (A5) in Appendix A1 in Payne & Melatos (2004), we know that

$$\psi = \int (G^* f)\mathrm{d}V + \int \hat{n}.(-G^*(\vec{\nabla}\psi) + \psi(\vec{\nabla}G^*) - G^*\psi\vec{b})\,\mathrm{d}S, \qquad \text{(B1)}$$

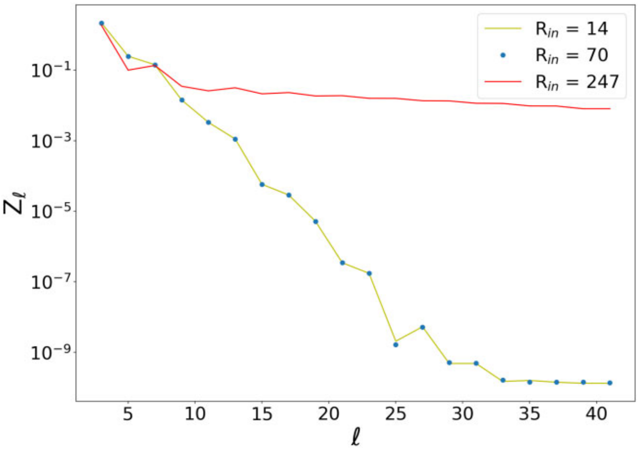

Figure B1. Plot of Z_ℓ (equation B6) versus ℓ for different values of inner radius. Here, the outer boundary is at 250 cell number. Unless the inner radius is selected closer to the outer boundary, higher multipole moments do not contribute significantly to the series solution for CFB.

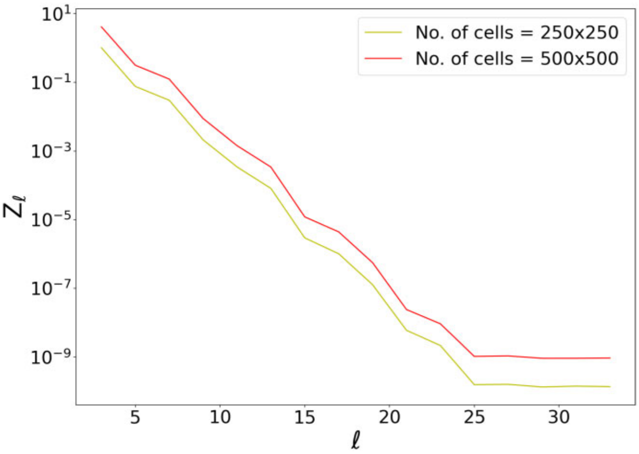

Figure B2. Plot of Z_ℓ (equation B6) versus ℓ for different values of resolution. Result is not affected by resolution.

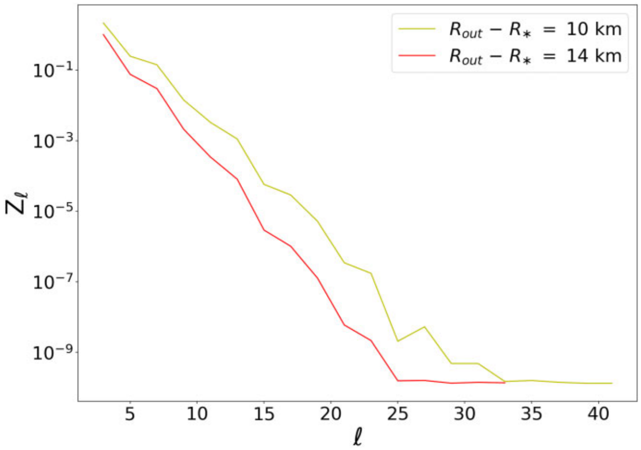

Figure B3. Plot of Z_ℓ (equation B6) versus ℓ for different values of outer boundary. A larger outer boundary requires lesser multipole terms in the series solutions for the same accuracy.

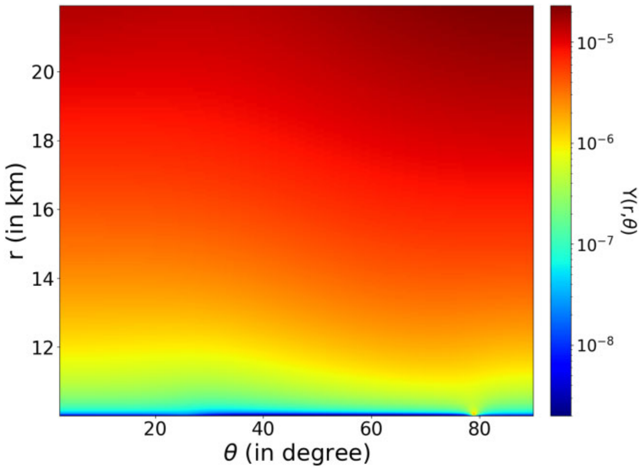

Figure B4. Relative difference between the solution using our new CFB condition and a Greens function based boundary condition. The maximum relative difference is lower than 10^{-4}.

where G^* is the greens function for the adjoint operator, and $\vec{b}$ is calculated using L^*. We need to find the value of ψ at the outer boundary ($R_{\rm out}$) at each step of the iteration. The above solution is valid for all regions. In order to evaluate the outer boundary independently at each iteration step of the SOR solver, we choose a source-free region ($f = 0$) above the mound. This implies a domain extending radially from an inner boundary $r = R_{\rm in}$ to $r = \infty$ and $\theta \in (0^0, 90^0)$. Appropriate constraints on the choice of $r = R_{\rm in}$ are discussed at the end of this subsection. Therefore, only the boundary terms contribute and we can write

$$\psi = \int \hat{n}.(-G^*(\vec{\nabla}\psi) + \psi(\vec{\nabla}G^*) - G^*\psi\vec{b})\,{\rm d}S.$$

$$\psi = \int [-(\hat{r}.(-G^*(\vec{\nabla}\psi) + \psi(\vec{\nabla}G^*) - G^*\psi\vec{b}))_{R_{\rm in}} + (\hat{r}.(-G^*(\vec{\nabla}\psi) + \psi(\vec{\nabla}G^*) - G^*\psi\vec{b}))_\infty]\,{\rm d}S.$$

At $r = R_{\rm in}$, $\psi = \psi(R_{\rm in}, \theta)$ (value of ψ from the previous iteration) and $G^* = 0$,

At $r = \infty$, $\psi = 0$ and $G^* = 0$.

Thus,

$$\psi = \int \left(-\psi(R_{\rm in}, \theta)\left(\frac{\partial G^*}{\partial r}\right)_{R_{\rm in}}\right).{\rm d}S.$$

$$\psi(r', \theta') = \int \left(-\psi(R_{\rm in}, \theta)\left(\frac{\partial G^*(r, \theta, r', \theta')}{\partial r}\right)_{R_{\rm in}}\right).R_{\rm in}^2 \sin\theta\,{\rm d}\theta\,{\rm d}\phi.$$

Differentiating G^* previously calculated (equation A16 in appendix A1) by Payne & Melatos (2004) and writing its value at $R_{\rm in}$, we get

$$\psi(r', \theta') = \int_0^\pi \psi(R_{\rm in}, \theta) R_{\rm in}^2 \sin\theta \times \sum_{\ell=1}^{\infty} \frac{(2\ell+1) R_{\rm in}^{\ell-2} P_\ell^1(\cos\theta) P_\ell^1(\cos\theta')\sin\theta'}{2\ell(\ell+1) r'^{(\ell)} \sin\theta}\,{\rm d}\theta. \tag{B2}$$

$$\psi(r', \theta') = \sin\theta' \sum_{\ell=1}^{\infty} \left(\frac{(2\ell+1)P_\ell^1(\cos\theta')}{2\ell(\ell+1)}\left(\frac{R_{\rm in}}{r'}\right)^\ell \times \int_0^\pi \psi(R_{\rm in}, \theta) P_\ell^1(\cos\theta)\,{\rm d}\theta\right). \tag{B3}$$

The above equation is used to calculate ψ at $R_{\rm out}$, which is the outer radius of the GS simulation domain. When ψ is symmetric about $\theta = \pi/2$ (not true for quadrudipolar field) i.e for $\psi(R_{\rm in}, \theta) = \psi(R_{\rm in}, \pi - \theta)$, equation can be simplified to

$$\psi(r', \theta') = \sin\theta' \sum_{\ell=1}^{\infty} \left(\frac{(2\ell+1)P_\ell^1(\cos\theta')}{2\ell(\ell+1)}\left(\frac{R_{\rm in}}{r'}\right)^\ell \times \int_0^{\frac{\pi}{2}} \psi(R_{\rm in}, \theta) P_\ell^1(\cos\theta)(1 + (-1)^{\ell+1})\,{\rm d}\theta\right). \tag{B4}$$

For this case, series in ψ admits only odd 'ℓ' values ($\ell = 1, 3, 5, 7.....$). To find ψ numerically, we need to choose an $\ell_{\rm max}$ up to which the series calculation should be done based on desired accuracy. Thus for dipolar inner boundary case, this equation can be written as

$$\psi(r', \theta') = \sum_{\ell=1}^{\ell_{\rm max}} \left(\frac{(2\ell+1)P_\ell^1(\cos\theta')}{2\ell(\ell+1)}\left(\frac{R_{\rm in}}{r'}\right)^\ell \sin\theta' \times \int_0^1 \frac{\psi(R_{\rm in}, \theta) P_\ell^1(\cos\theta)(1 + (-1)^{\ell+1})}{\sqrt{1 - \cos^2\theta}}\,{\rm d}(\cos\theta)\right). \tag{B5}$$

To calculate the solution at the outer boundary, value of $r' = R_{\rm out}$. Different value of $R_{\rm in}$ needs to be selected as far away from $R_{\rm out}$ as possible, to make sure the term $\left(\frac{R_{\rm in}}{R_{\rm out}}\right)^\ell$ reduces drastically for values of $\ell > \ell_{\rm max}$, increasing the accuracy of this calculation. Thus, we suggest choosing $R_{\rm in}$ near the top of the mound in vacuum.

B2 Selection of $\ell_{\rm max}$

A value of $\ell_{\rm max}$ needs to be selected to truncate the series calculation for the CFB condition. To decide $\ell_{\rm max}$, multiple solutions are calculated with the series for CFB condition truncated at multiple values of ℓ. ψ_ℓ is thus the solution calculated with the series for the CFB condition truncated at ℓ. Z_ℓ is a parameter used to compare solutions and finalize the value of $\ell_{\rm max}$:

$$Z_\ell = \sum_{i,j} |\psi_\ell(r_i, \theta_j) - \psi_{\ell-2}(r_i, \theta_j)|. \tag{B6}$$

B2.1 Different value of $R_{\rm in}$

To test the effect of different values of the parameter $R_{\rm in}$ (radius at which solution is used to calculate and update the outer radial boundary) on $\ell_{\rm max}$, multiple simulations are setup for a 4 m accretion mound with surface magnetic field strength 10^9 G, truncation angle 45.5^0, number of points 250×250 and outer radius above the surface ($R_{\rm out} - R_*$) 10 km. Plots of Z_ℓ for three different values of $R_{\rm in}$ i.e. 14 ($R_{\rm in} - R_* = 4.3$ m) (14 means 14th point), 70 ($R_{\rm in} - R_* = 56.8$ m), 247 ($R_{\rm in} - R_* = 8.7$ km) have been represented in Fig. B1. It is apparent that unless $R_{\rm in}$ is selected near the outer radial boundary (like 247), Z_ℓ converges at $\ell = 33$ for these parameters.

B2.2 Effect of resolution

To test the effect of resolution on $\ell_{\rm max}$, multiple simulations are setup for a 4 m accretion mound with surface magnetic field strength 10^9 G, truncation angle 45.5^0, $R_{\rm in}$ close to the top of the mound and outer radius above the surface ($R_{\rm out} - R_*$) 14 km. Behaviour of Z_ℓ for two different resolutions have been plotted in Fig. B2. Value of Z_ℓ is higher for a higher resolution as the addition takes place over larger number of cells. From Fig. B2, we can conclude that resolution affects the value of Z_ℓ but not the value of ℓ at which Z_ℓ converges.

B2.3 Effect of changing outer boundary

To test the effect of different values of the outer radius on $\ell_{\rm max}$, multiple simulations are setup for a 4 m accretion mound with surface magnetic field strength 10^9 G, truncation angle 45.5^0, number of points 250×250, and $R_{\rm in}$ close to the top of the mound. Plots of Z_ℓ for two different values of outer radius above the surface ($R_{\rm out} - R_*$), i.e. 10 km and 14 km are represented in Fig. B3. We can conclude that a larger value of outer radius makes Z_ℓ converge at a lower value of ℓ. A larger mass or a lower dipole moment does not affect the behaviour of Z_ℓ with $\ell_{\rm max}$. For almost all the simulations performed in this work (unless explicitly mentioned), the outer radius above the surface ($R_{\rm out} - R_*$) is 12 km and $R_{\rm in}$ is close to the top of the mound, thus from all the tests performed above, $\ell_{\rm max}$ was chosen to be 33 (convergence for outer radius above the surface ($R_{\rm out} - R_*$) 10 km).

B3 Checking with Greens function volume boundary condition

Instead of using an arbitrary $R_{\rm in}$ to evaluate the outer boundary, we can use the Greens function formalism to evaluate the outer boundary using all the cells with non-zero density or non-zero source function. Fujisawa et al. (2022) have used such an integral form to solve for the whole simulation domain. ψ at the outer boundary is calculated using ψ values of the whole simulation domain as follows:

$$\psi(R_{\rm out}, \theta') = \frac{\psi^* \sin^2\theta' R_*}{R_{\rm out}} + \sum_{\ell=1,3,5...}^{\infty} \frac{\sin\theta' P_\ell^1(\cos\theta')}{\ell(\ell+1)} \times R_{\rm out}^{-\ell} \left(\int_0^{\frac{\pi}{2}} \int_{R_*}^{R_{\rm out}} r^{\ell+1} \left(\left(\frac{R_*}{r}\right)^{2\ell+1} - 1 \right) \times P_\ell^1(\cos\theta) K(\psi, r, \theta)\, {\rm d}r\, {\rm d}\theta \right). \quad \text{(B7)}$$

Comparing the solution by applying the above boundary condition, with a solution with our simpler boundary condition with an arbitrary $R_{\rm in}$ closer to the top of the mound, we find that the maximum absolute relative difference $Y(r, \theta)$ between the solutions is lower than 5×10^{-5}, for resolution 600×600 and normalized outer dipole moment 0.83. The absolute relative difference $Y(r, \theta)$ between the two solutions is plotted in Fig. B4 ($r_c = 10^2$ m, $B_d = 10^{12}$ G, $\theta_t = 84^0$). In the case where the whole simulation domain includes significant screening currents or toroidal fields, the volume terms with the source function need to be included in the greens function formalism along with the boundary terms to calculate the solution at the outer radial boundary.

APPENDIX C: NUMERICAL MAXIMUM MASS

C1 NMM for fixed θ_t and fixed B_d

Earlier studies (Hameury et al. 1983; Payne & Melatos 2004; Mukherjee & Bhattacharya 2012) have shown that numerically converged GS solutions can be obtained up to a maximum confined mass, beyond which closed field lines start to appear, resulting in magnetic loops. However, it remains unclear whether such occurrences are due to the specific choice of profile functions or lack of resolution. In order to test such scenarios we have run a suite of models with fixed B_d and θ_t, but varying r_c. Solutions for ring-shaped mound profile keep spreading as shown in Section 4.2.1. It is necessary to check the validity of these solutions. We apply a perturbation based test, as discussed below:

(i) Use an initial dipolar guess and obtain a solution $\psi(r, \theta)$ from our prescribed numerical method.

(ii) Now, use $\psi(r, \theta) \times (1.0 + q \times u(r, \theta))$ (q is assumed to be 10, while $u(r, \theta)$ is a random number from a uniform distribution between 0 and 1 drawn for each point of the grid) as an initial guess and obtain a solution $\psi_{\rm pert}(r, \theta)$ from the same prescribed numerical method.

(iii) Compute

$$Y(r, \theta) = \frac{|\psi(r, \theta) - \psi_{\rm pert}(r, \theta)|}{\psi(r, \theta)}, \quad \text{(C1)}$$

the difference of the perturbed solution from the original to compare $\psi(r, \theta)$ and $\psi_{\rm pert}(r, \theta)$.

(iv) If $MAX(Y(r, \theta))$ is larger than 10^{-3}, then a non-unique solution has been obtained by using a different guess but evaluated with the same method. Thus, this solution is deemed invalid.

In general, we find that with an increase in r_c for fixed θ_t and B_d, after a certain height, $MAX(Y(r, \theta))$ transitions from a low value (e.g. $\sim 10^{-11}$) to a high value (viz. $> 10^{-3}$). This indicates a strong deviation from the original solution, implying multiple branches or families of potential solutions, resulting in non-uniqueness. We deem such solutions invalid.

An example of this behaviour has been plotted in Fig. C1. The left panels show the $Y(r, \theta)$ and the solutions for a mound with $r_c = 11.33$ m. However, increasing r_c by 0.01 m, the perturbation analysis shows very large deviations from the unperturbed solution. We call the last valid solution mass (i.e. in this case for $r_c = 11.33$ m) as the NMM. All the solutions presented in this paper are numerically valid.

Now, the interesting question is ‘Why does the numerical method converge, but presents a non-unique solution for a different guess?’. This is because there are large gradients in ψ near the truncation angle θ_t, which increase with increasing r_c. Eventually, mounds with a perturbed starting guess solution tend to diffuse beyond the solutions obtained from a dipolar guess value, making the solution invalid, as presented in Fig. C2. This is likely mediated by numerical resistivity. For low resolutions such as 600×600, numerical instabilities make closed loops of magnetic field lines near the truncation angle for

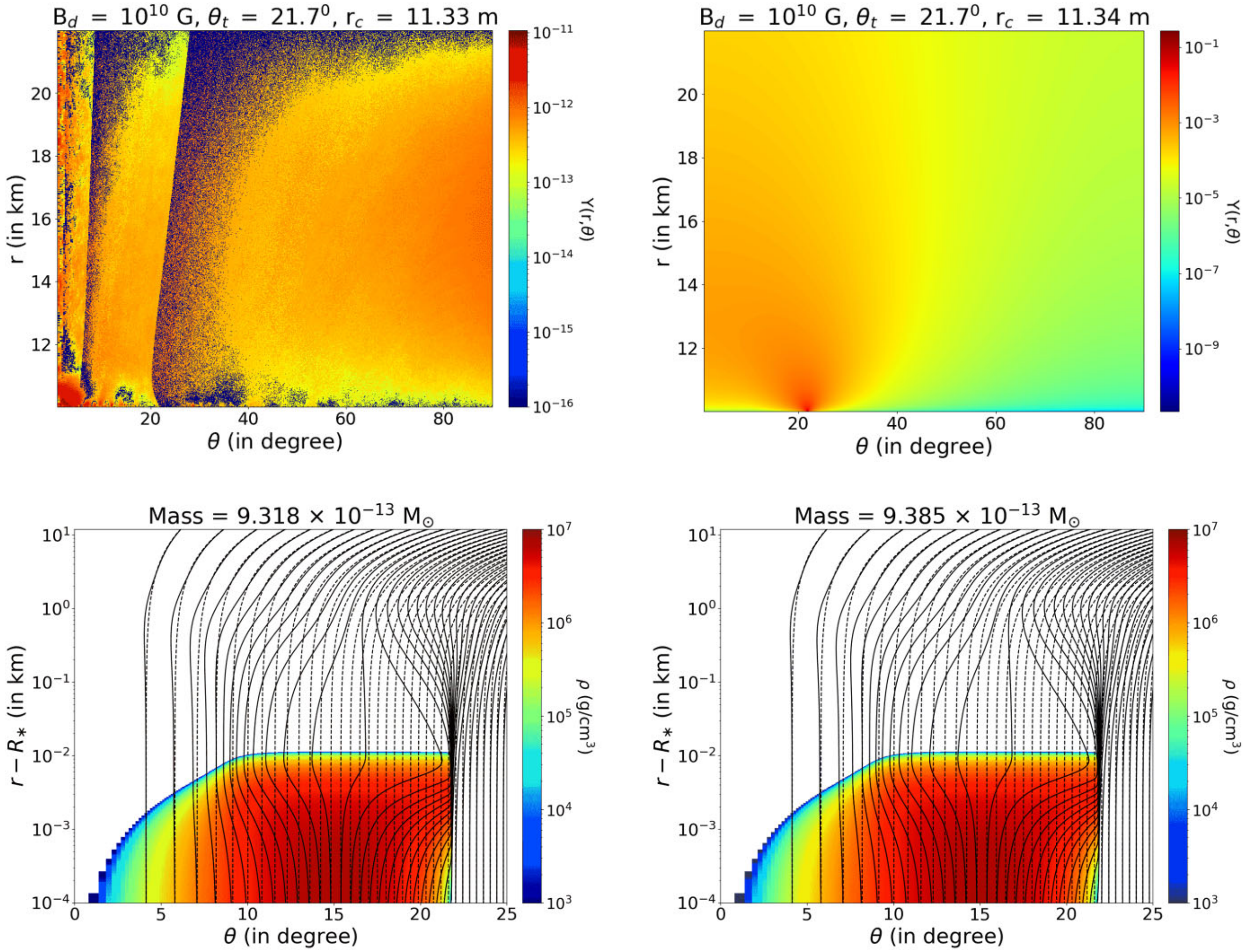

Figure C1. Colourmap of $Y(r, \theta)$ between perturbed and unperturbed solution for parameters $B_d = 10^{10}$ G, $\theta_t = 21.7^0$, $r_c = 11.33$ m, mass $= 9.318 \times 10^{-13}$ $\mathrm{M}_\odot$ (top left) and density profile, magnetic field lines (solid), and dipolar magnetic field lines (dashed) for the same parameters (bottom left). Maximum $Y(r, \theta)$ is lower than 10^{-10}, thus even with the perturbed guess, the code converges to the same solution. Colourmap of $Y(r, \theta)$ between perturbed and unperturbed solution for parameters $B_d = 10^{10}$ G, $\theta_t = 21.7^0$, $r_c = 11.34$ m, mass $= 9.385 \times 10^{-13}$ $\mathrm{M}_\odot$ (top right), density profile, magnetic field lines (solid), and dipolar magnetic field lines (dashed) for the same parameters (bottom right). Maximum $Y(r, \theta)$ is greater than 0.1, i.e. the code converges to a different solution for a perturbed guess.

a starting solution with a perturbed ψ, as presented in Fig. C3 in Appendix C2. Closed loops have also been reported in earlier studies (Hameury et al. 1983; Payne & Melatos 2004; Mukherjee & Bhattacharya 2012). However, such cases were either due to lack of resolution (Appendix C2) or the choice of the profile function (i.e. closed loops in Fig. 5). For higher resolutions, the large gradients in ψ near θ_t are well resolved keeping the solution valid, allowing the matter to continue to spread towards the equator with an increase in r_c (Section 4.2.1).

Since diffusion of matter or formation of closed loops near θ_t deems the solution invalid, and is dependent on resolution, the value of NMM is resolution dependent. Table C1 lists down the NMM for different simulation domain resolutions.

Since the latitudinal direction is represented in the $\cos\theta$ coordinates, the regions near the equator are better resolved in θ than the poles. Thus, for the same resolution, a solution with a larger θ_t naturally favours a larger NMM for our choice of coordinates, because the resolution in θ increases as the value of θ increases from 0^0 to 90^0. Once a solution is deemed numerically valid, dynamical stability of the solution needs to be probed.

C2 NMM resolution dependence

It has been established in the above Section C1 and by Table C1 that NMM of the mounds defined by our criteria depends on resolution.

For low resolutions, closed loops form after solving with a perturbed guess near the truncation angle due to numerical resistivity. For a 600 × 600 simulation, Fig. C3 shows the solution derived from a dipolar guess before perturbing and the solution derived from a perturbed guess of the previous solution. Multiple closed magnetic loops at the right of the truncation angle are visible in the bottom plot of Fig. C3.

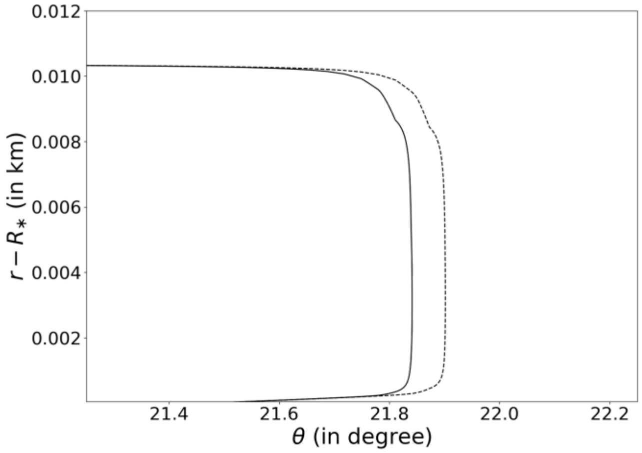

Figure C2. Contours for density: $\rho = 10^5$ g/cm^3 for GS run with parameters corresponding to the rightmost plot in Fig. C1. The solution ψ with a dipolar guess is presented in a solid line and the solution $\psi_{\rm pert}$ with a perturbed guess in a dashed line. The perturbed input leads to spreading of matter beyond the first solution, resulting in strong deviation between the two solutions.

Table C1. Resolution versus maximum mass for parameters $B_d = 10^9$ G and $\theta_t = 45.5^0$.

Resolution	Maximum mass ($M_\odot$)
700 × 700	3.3363×10^{-13} $M_\odot$
800 × 800	3.4282×10^{-13} $M_\odot$
1000 × 1000	3.4421×10^{-13} $M_\odot$
2000 × 2000	3.6073×10^{-13} $M_\odot$
3000 × 3000	4.1566×10^{-13} $M_\odot$
5000 × 5000	5.65×10^{-13} $M_\odot$

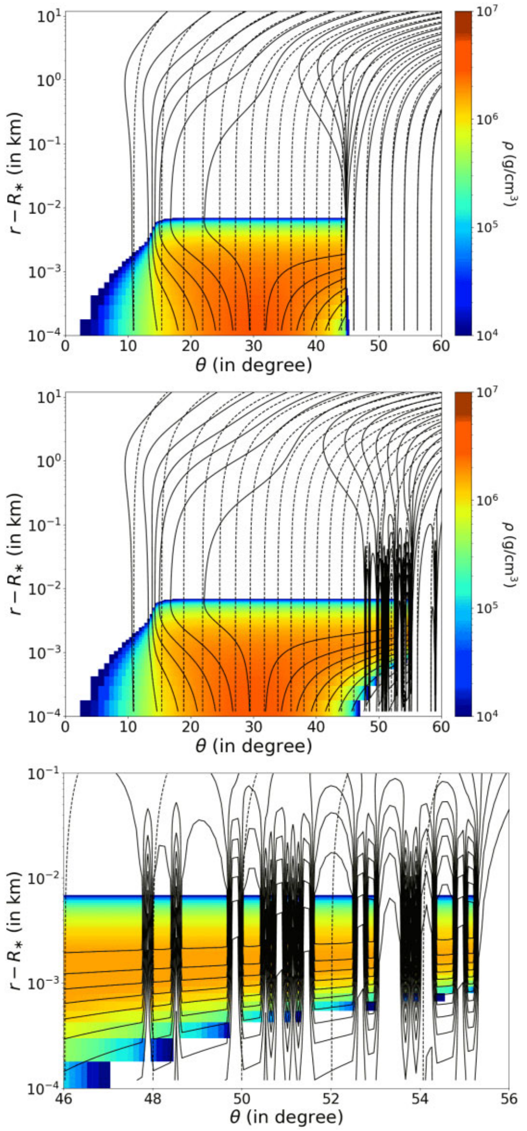

Figure C3. Plot of density profile and magnetic field lines (solid) for resolution 600 × 600, parameters $B_d = 10^9$ G, $r_c = 7$ m, and $\theta_t = 45.5^0$. Solution from a dipolar guess (top) and the Solution from a perturbed guess (middle) are plotted here. Closed magnetic loops are clearly visible in the bottom plot (close-up of the middle plot).

This paper has been typeset from a TEX/LATEX file prepared by the author.